

# Open Research Online

---

The Open University's repository of research publications  
and other research outputs

## Localised heating and intensive magmatic conditions prior to the 22–23 April 2015 Calbuco volcano eruption (Southern Chile)

### Journal Item

#### How to cite:

Morgado, Eduardo; Morgan, Daniel J.; Harvey, Jason; Parada, Miguel-Ángel; Castruccio, Angelo; Brahm, Raimundo; Gutiérrez, Francisco; Georgiev, Bogomil and Hammond, Samantha J. (2019). Localised heating and intensive magmatic conditions prior to the 22–23 April 2015 Calbuco volcano eruption (Southern Chile). *Bulletin of Volcanology*, 81(4), article no. 24.

For guidance on citations see [FAQs](#).

© 2019 The Authors



<https://creativecommons.org/licenses/by/4.0/>

Version: Version of Record

Link(s) to article on publisher's website:

<http://dx.doi.org/doi:10.1007/s00445-019-1280-2>

---

Copyright and Moral Rights for the articles on this site are retained by the individual authors and/or other copyright owners. For more information on Open Research Online's data [policy](#) on reuse of materials please consult the policies page.

---

[oro.open.ac.uk](http://oro.open.ac.uk)



# Localised heating and intensive magmatic conditions prior to the 22–23 April 2015 Calbuco volcano eruption (Southern Chile)

Eduardo Morgado<sup>1,2</sup> · Daniel J. Morgan<sup>1</sup> · Jason Harvey<sup>1</sup> · Miguel-Ángel Parada<sup>2,3</sup> · Angelo Castruccio<sup>2,3</sup> · Raimundo Brahm<sup>2,3,4</sup> · Francisco Gutiérrez<sup>5</sup> · Bogomil Georgiev<sup>1</sup> · Samantha J. Hammond<sup>6</sup>

Received: 6 August 2018 / Accepted: 20 February 2019 / Published online: 13 March 2019  
© The Author(s) 2019

## Abstract

Calbuco volcano is a Late Pleistocene composite stratovolcano and member of the Southern Volcanic Zone of the Chilean Andes (41°19'S, 72°36'W). It lies ~20 km west of the Liquiñe–Ofqui Fault Zone, but is not located directly upon any major regional structures. During April 2015, a sub-Plinian eruption occurred, with a bulk erupted volume of ~0.3–0.6 km<sup>3</sup> (~0.1–0.2 km<sup>3</sup> DRE). The eruption was a rapid-onset event that produced highly crystalline products (from 40 to 60 vol.%) including the mineral phases: plagioclase, clinopyroxene, orthopyroxene, amphibole, olivine, apatite, ilmenite, titanomagnetite and chalcopyrite. An upper-crustal reservoir is inferred using available geophysical data combined with amphibole geobarometry. Consideration of textural features, including high crystallinity, complex mineral zonation, crystal clots and interstitial glass between crystals from clots, suggests the presence of a mush zone within this reservoir. From the nine collected samples, whole-rock chemistry and an array of geothermometers (amphibole, amphibole-plagioclase, two-pyroxenes and Fe–Ti oxides) gave similar results for all samples possessing ~40 vol.% of crystals, with the exception of the sample Cal-160 (~60 vol.% crystallinity), which is slightly more evolved and yields lower temperatures for all geothermometers. By comparing temperatures calculated in sample Cal-160 using pairs of ilmenite-titanomagnetite core compositions with those calculated using rim compositions, we observe a late-stage temperature increase of between 70 and 200 °C. We suggest that this local-scale heating event was at least partly responsible for triggering the eruption. Our data suggest that the bulk of the erupted magma was derived from a relatively uniform (970–1000 °C), crystal-rich magma mass. Sample Cal-160 was derived from a cooler environment (910–970 °C), where it was subjected to pre-eruptive heating to temperatures considerably higher than those observed in associated, erupted magmas (up to 1070 °C). This requires the involvement of a hot, presumably mafic magma injection at the base of a shallow, crystal-rich reservoir, though the mafic magma was not itself erupted. The localised nature of interaction and rapidity of eruption onset have implications for potential future hazards at Calbuco volcano.

**Keywords** Calbuco volcano · Magma heating · Geothermobarometry · Crystal mush

---

Editorial responsibility: L. Pioli

**Electronic supplementary material** The online version of this article (<https://doi.org/10.1007/s00445-019-1280-2>) contains supplementary material, which is available to authorized users.

✉ Eduardo Morgado  
eeeem@leeds.ac.uk

<sup>1</sup> Institute of Geophysics and Tectonics, School of Earth and Environment, University of Leeds, Leeds LS2 9JT, UK

<sup>2</sup> Centro de Excelencia en Geotermia de los Andes (CEGA-FONDAP 15090013), Santiago, Chile

<sup>3</sup> Departamento de Geología, Facultad de Ciencias Físicas y Matemáticas, Universidad de Chile, Santiago, Chile

<sup>4</sup> Volcanic Risk Solutions, Institute of Agriculture and Environment, Massey University, Palmerston North 4442, New Zealand

<sup>5</sup> GeoExpedition, Las Barrancas 25, Pirque, 9480000 Santiago, Chile

<sup>6</sup> Environment, Earth and Ecosystems, The Open University, Milton Keynes MK7 6AA, UK

## Introduction

Within the continental crust, magma reservoirs are considered to be represented by both *magma chambers*, these being defined as continuous, melt-rich, lenticular regions where the magma is fluid and eruptible and within which magma crystallinity is < 45 vol.%, and *crystal mushes*, i.e. a body with a rigid crystal framework and crystallinity > 45% (Marsh 1989, 1996; Hildreth 2004; Bachmann and Bergantz 2008). Crystallinities > 45 vol.% are associated with rheological properties which impede convection processes (e.g. Bachmann and Bergantz 2004, 2008; Huber et al. 2010a; Burgisser and Bergantz 2011; Parmigiani et al. 2014). These reservoirs exist as shallow magma reservoirs ( $\leq 10$  km depth) and may evolve over long cooling periods to become plutons (e.g. Koyaguchi and Kaneko 1999; Claiborne et al. 2010; Cooper and Kent 2014; Molina et al. 2015; Szymanowski et al. 2017; Cooper et al. 2017).

Sample mineralogy and whole-rock chemistry are usually studied together in order to understand magma reservoirs. Mineral compositions, however, yield diverse information regarding crystallisation conditions, crystal re-equilibration and timescales, which depend upon the diffusion kinetics of their constituent elements. For example, major elements of Fe–Ti oxides show much higher interdiffusivity (Aragon et al. 1984; Aggarwal and Dieckmann 2002a, b) than those of silicate phases (e.g. plagioclase, Grove et al. 1984; clinopyroxene, Müller et al. 2013; orthopyroxene, Ganguly and Tazzoli 1994, Dohmen et al. 2016; and olivine, Dohmen and Chakraborty 2007a, b). Therefore, Fe–Ti oxides equilibrate much faster than silicate phases, typically recording magma eruption temperatures. By contrast, the silicates can provide information on earlier stages of the magmatic history with little re-equilibration. This study reports whole-rock chemistry, mineral chemistry, textural features and calculations of pre-eruptive intensive conditions (geothermometry, geobarometry and oxybarometry) derived from fall deposits of the sub-Plinian eruption of Calbuco volcano (Southern Chile), which occurred on 22–23 April 2015. In doing so, we recognise and quantify a local-scale heating event prior to the eruption, which we interpret to represent an input of new, hot magma beneath an inferred shallow magma reservoir including a mush zone with limited mixing or interaction between the overlying reservoir and the new magma input.

## Geological setting

### Calbuco volcano

Calbuco volcano (41°19'S, 72°36'W) is a Late Pleistocene–Holocene composite stratovolcano (López-Escobar et al. 1992) of the Central Southern Volcanic Zone of the Andes.

Its summit is 2003 m above sea level and the basal area of the volcano is 150 km<sup>2</sup> (Sellés and Moreno 2011). Calbuco has been catalogued as the third most dangerous Chilean volcanic system (Lara et al. 2011; SERNAGEOMIN 2017). It is located ~20 km west of the Liquiñe–Ofqui Fault Zone (LOFZ; Fig. 1), a major dextral, transpressive strike-slip structure of the Southern Volcanic Zone (Cembrano et al. 1996, 2000). According to Sellés and Moreno (2011), however, Calbuco volcano is not itself located directly upon any major regional structure. The basement of the area is composed of late Palaeozoic metamorphic rocks from the Sotomó–Chaiquenes (Thiele et al. 1985) and Lengua (SERNAGEOMIN – BRGM 1995) metamorphic complexes and later plutonic rocks, which are members of the Miocene plutonic belt of the Northern Patagonian Batholith (López-Escobar et al. 1992; Adriasola et al. 2006). The Calbuco volcanic edifice immediately overlies Early Pleistocene volcanic sequences (the Hueñuhueñu and Reloncaví strata; López-Escobar et al. 1995b).

The construction of the Calbuco edifice is ~300 ka old (Sellés and Moreno 2011) and is characterised by alternations between lava flows (basaltic to basaltic andesitic with rare dacite), andesitic to dacitic domes and layers of pyroclastic tephra, block and ash flows, and deposits from hot and cold lahars (López-Escobar et al. 1992, 1995a, b; Petit-Breuilh 1999; Moreno et al. 2006; Stern et al. 2007; Castruccio et al. 2010; Sellés and Moreno 2011; Watt et al. 2011; Daga et al. 2014). The dominantly andesitic composition of its products (with high Sr isotope ratios and low Nd isotope ratios; López-Escobar et al. 1995b), combined with the presence of crustal xenoliths and magmatic amphibole phenocrysts, make this volcano notably more evolved by comparison to other nearby volcanic complexes such as Osorno volcano (Parada 1990; López-Escobar et al. 1992, 1995a, b; Hickey-Vargas et al. 1995). The long-term evolution of the products of Calbuco volcano has been divided into four units (Lahsen et al. 1985; López-Escobar et al. 1992, 1995b; Sellés and Moreno 2011); details of the three prehistoric units (Calbuco 1, 2 and 3) are shown in Table 1 and details of the historical unit (Calbuco 4) are shown in Table 2.

### The April 2015 Calbuco eruption

During 22–23 April 2015, two sub-Plinian eruptive events occurred at Calbuco volcano. The first eruptive pulse started on 22 April at 17:50 local time (20:50 UTC) and the second started on 23 April at 01:00 local time (04:00 UTC) (SERNAGEOMIN 2015a, b, c, d). These pulses produced eruptive columns with heights exceeding 15 km (SERNAGEOMIN 2015e; Romero et al. 2016; Van Eaton et al. 2016). Van Eaton et al. (2016) reported pyroclastic density currents (PDCs) at the end of the first eruptive pulse, with the largest PDCs occurring at the onset of the second eruptive

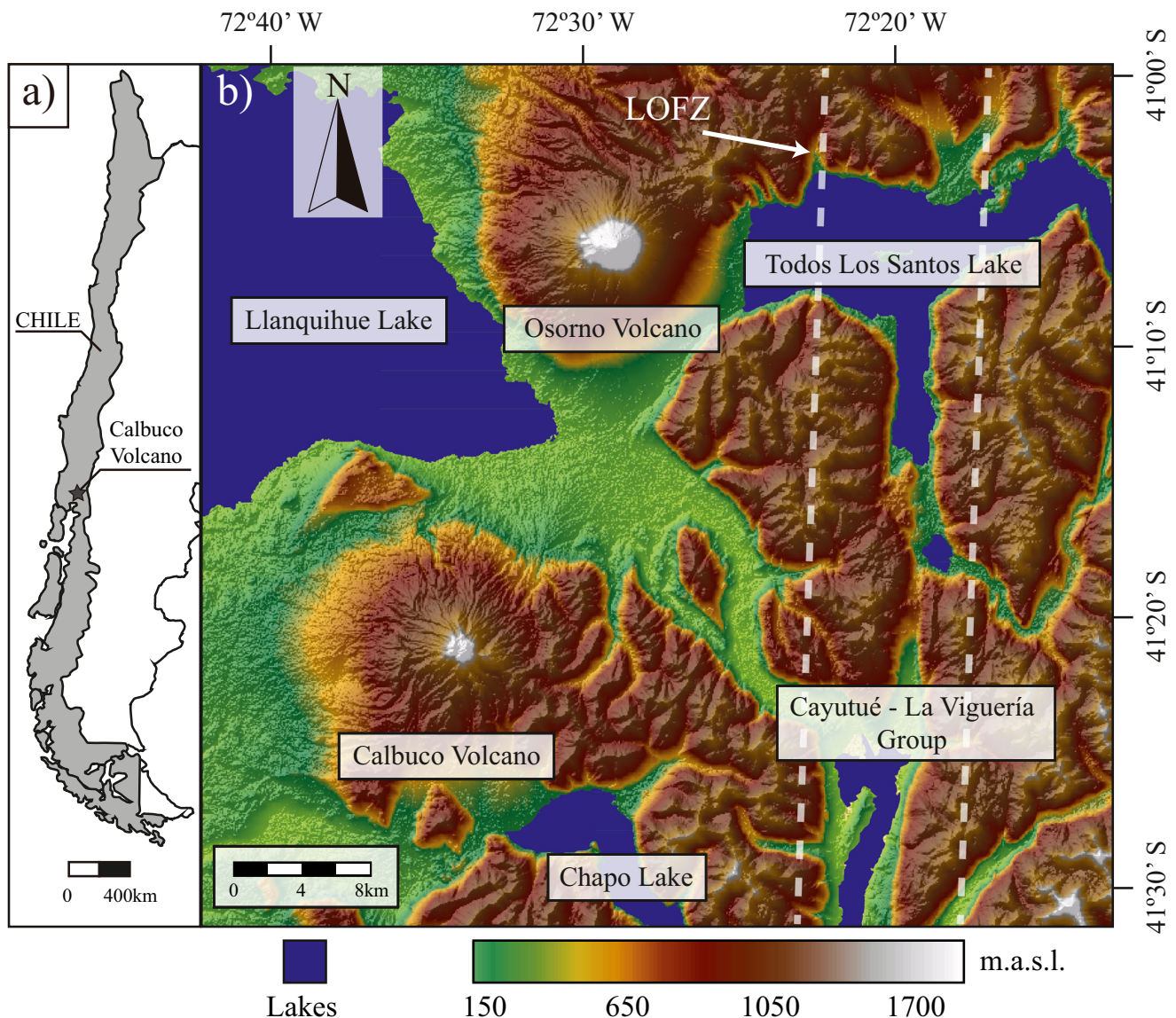


**Fig. 1** (a) Location of Calbuco volcano with respect to Chile and (b) regional map of Calbuco volcano on shaded relief/Digital Elevation Model. Calbuco is located between Llanquihue and Chapo lakes, ~ 20 km west from the Liquiñe-Ofqui Fault Zone (LOFZ, dashed white

line). The Advanced Spaceborne Thermal Emission and Reflection Radiometer (ASTER) Global Digital Elevation Model (GDEM) image was obtained via EarthExplorer, USGS (<http://earthexplorer.usgs.gov>)

pulse. During the entire eruption sequence, primary and secondary lahars were generated on the S, N and NE flanks and no lava flows were emitted (Castruccio et al. 2016).

Several authors have estimated the bulk erupted volume during the eruption:  $0.27 \text{ km}^3$  ( $0.11\text{--}0.13 \text{ km}^3$  dense rock equivalent, DRE; Romero et al. 2016),  $0.56 \pm 0.28 \text{ km}^3$  ( $0.18 \pm 0.09 \text{ km}^3$  DRE; Van Eaton et al. 2016),  $0.38 \pm 0.1 \text{ km}^3$  ( $0.15 \text{ km}^3$  DRE; Castruccio et al. 2016) and  $0.37\text{--}0.6 \text{ km}^3$  (Delgado et al. 2017). The eruption had a volcanic explosivity index (VEI) of 4, based on the estimated bulk volumes (Romero et al. 2016; Van Eaton et al. 2016). Most of the products were erupted during the first pulse (Romero et al. 2016).

In terms of precursory activity, Valderrama et al. (2015) reported 147 seismic events occurring from 1 January to 21 April 2015, of which 142 were volcano-tectonic (VT, related to fracturing of the wall rock) and 5 were long-period (LP, related to collapse of gas bubbles in rising magma or fluid movement events). From February 2015, there was an increase in low-magnitude VT seismic activity and later, during 22 April, a seismic swarm of 140 VT events was recognised starting just 3 h before the eruption onset (SERNAGEOMIN 2015f). The first LP events were registered at 16:34 local time (19:34 UTC, ~ 1.5 h before the eruption) and during the second pulse there was an increase in the number of VT seismic events (SERNAGEOMIN 2015g). Although no



**Table 1** Main features of the different prehistorical units of Calbuco volcano

Unit	Description	Mineralogy <sup>b</sup>
Calbuco 1 (340–110 ka)	Unit composed mainly of andesite-basalt and scarce basalt lavas (50–56.6 wt.% SiO <sub>2</sub> ) interbedded with volcanoclastic deposits. The deposits lie in disconformity over plutonic and metamorphic basement as well as volcanic and volcanoclastic deposits (Estratos de Hueñuhueñu, 1.4 Ma; Lahsen 1985). Sellés and Moreno (2011) have recognised gabbro and pyroxenite xenoliths	Plagioclase, clinopyroxene, orthopyroxene, olivine <sup>a</sup> , amphibole
Calbuco 2 (110–14.5 ka)	Unit composed mainly of andesitic lavas (56–61 wt.% SiO <sub>2</sub> ) interbedded with pyroclastic flows, fall deposits and laharc breccias. Occasionally can be found andesitic dome lavas, pyroclastic deposits and volcanic avalanches (Sellés and Moreno 2011)	Plagioclase, clinopyroxene, orthopyroxene, olivine <sup>a</sup>
Calbuco 3 (~ 14 ka to 1893 AD)	Unit composed of lavas (mainly of andesitic composition), pyroclastic rocks and laharc breccias. Most of the samples have andesite-basaltic and andesitic composition (55–60 wt.% SiO <sub>2</sub> ). Scarce dacites (64.5 wt.% SiO <sub>2</sub> ) also have been recognised (Sellés and Moreno 2011)	Plagioclase, clinopyroxene, orthopyroxene, olivine <sup>a</sup>

<sup>a</sup> All the olivines were surrounded by a pyroxene crown

<sup>b</sup> According to Sellés and Moreno (2011)

deformation was recognised up to 1.5 days before the eruption, deflation was documented during the eruption (Delgado et al. 2017), which agrees with the contemporary tiltmeter information (Valderrama et al. 2015). According to Delgado et al. (2017) the deformation source models are consistent with a deflation between 8 and 11 km depth. The consequences of the eruption were not only local, where chemical-climate interaction modelling suggests that the 2015 Calbuco eruption led to an increase in the areal extent of the Southern ozone hole by  $4.5 \times 10^6$  km<sup>2</sup> (Ivy et al. 2017). Although on 30 April there was another eruptive pulse, this was a steam-

**Table 2** Main features of the historical products of Calbuco volcano

Year of the eruption	Description	Mineralogy
1893	A violent eruption started on February 1893 and finished during the last months of 1895 (Petit-Breuilh 1999). During October 1893 was the paroxysmal stage, when the eruptive column reached ~ 9 km height (VEI 3 estimated; Fischer 1893; Petit-Breuilh 1999)	—
1911	During 1911 and 1912, gas and ashes were erupted (Petit-Breuilh 1999)	—
1917	During April 1971, an eruption occurred with a lava flow, dome-cone and some lahars were associated. The lava flow had andesitic composition (59.3 wt.% SiO <sub>2</sub> ) and gabbroic and troctolitic clots were found (Sellés and Moreno 2011)	Plagioclase, orthopyroxene, amphibole, opaque
1929	During January 1929, 2.5-km-long (from the crater to NE direction) and 0.5-km-long (from the crater to SE direction) andesitic lavas (55.5 wt.% SiO <sub>2</sub> ). Some crystal mush xenolith of amphibole gabbros have been recognised (Sellés and Moreno 2011). Lahars were generated during the eruption flowing towards northwest (Petit-Breuilh 1999)	Plagioclase, pyroxenes, olivine <sup>a</sup> , amphiboles
1961	During February 1961, 4.6-km-long (NE direction) and 1.7-km-long (SE direction) andesitic lavas were erupted. As a consequence, some lahars and hot lahars were generated (Klohn 1963; Moreno et al. 2006; Castruccio et al. 2010). According to the morphological features of glassy particles, this eruption is associated to magma/water interactions (Daga et al. 2014). Also granulitic, gabbroic and noritic clots have been recognised (Hickey-Vargas et al. 1995; Moreno and Sellés 2011)	Plagioclase, clinopyroxene, orthopyroxene, olivine <sup>a</sup> , amphibole, quartz

<sup>a</sup>All the olivines were surrounded by a pyroxene crown

— No information available

driven eruption with little participation of fresh magma. The plume reached < 5 km above the vent with dispersion

towards the SE (SERNAGEOMIN 2015g; Van Eaton et al. 2016). The registered deformation during this eruptive event was negligible (Delgado et al. 2017).

## Analytical procedures

### Geochemistry

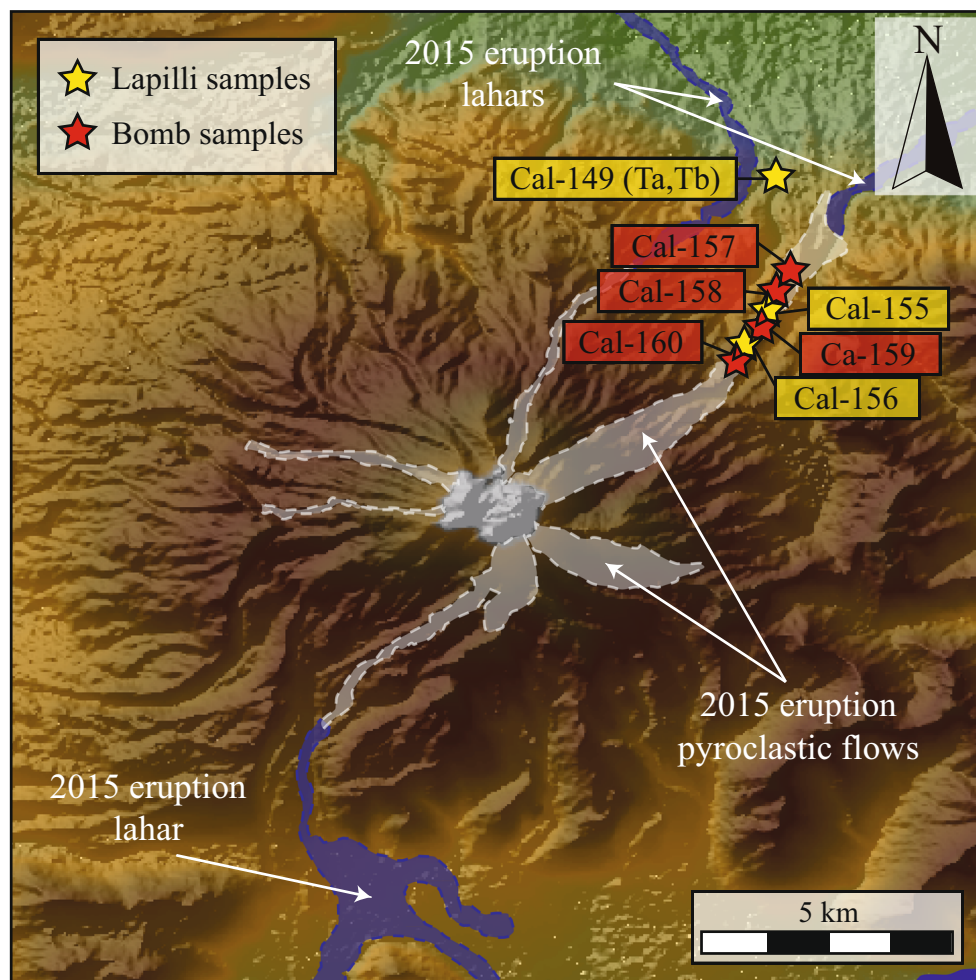
Nine samples (four lapilli-sized pyroclasts from fall deposits and five bombs from pyroclastic density current deposits) were collected from the products of the 2015 Calbuco eruption deposits from seven locations (Fig. 2). Whole-rock compositions of three lapilli and four bomb samples were analysed via XRF (for major elements) at Acme Analytical Labs (Vancouver, Canada) using OREAS-184 and SY-4 standards for all the major elements, and CCU-1D and OREAS-700 standards for FeO. Accuracy for major elements in all standards is better than 3% (relative) except for  $\text{TiO}_2$  in SY-4 which is 4.5% (relative) and  $\text{P}_2\text{O}_5$  in OREAS-184 and SY-4 which are 14% and 17% (relative), respectively. Trace element compositions were analysed

via ICP-MS at the Open University (Milton Keynes, UK) using the BHVO-2, JB-2 and AGV-1 standards. The reproducibility of analyses was better than 8% (relative;  $2\sigma$ ) and accuracy in the trace elements in JB-2 ( $n = 5$ ), BHVO-2 ( $n = 2$ ) and AGV-1 ( $n = 2$ ) is better than 10%, except in Ni (21% in AGV-1) and Pb (13% in BHVO-2).

The mineral chemistry analyses of amphibole, plagioclase, pyroxene, Fe–Ti oxide and olivine were measured using an electron microprobe (JEOL JXA8230) at Leeds Electron Microscopy and Spectroscopy Centre at the University of Leeds (Leeds, UK). Counting time is distributed equally between on-peak and background measurements, using the following conditions:

**Amphiboles** Major and minor element concentrations (Si, Ti, Al, Fe, Mn, Mg, Ca, Na, K, Cr, Cl and F) were measured in the cores of amphibole grains. The analytical conditions consisted of an accelerating potential of 20 keV and focused beam for all the elements. An electron beam current of 15 nA was used for Si, Ti, Al, Fe, Mn, Mg, Ca, Na, K and Cr, whereas a current of 100 nA was used for F and Cl. Counting times were 30 s for

**Fig. 2** Location of samples (lapilli and bombs) from the 2015 Calbuco eruption on shaded relief/Digital Elevation Model. Location of pyroclastic density currents (white) and lahars (blue) are based on Castruccio et al. (2016). The ASTER–GDEM Image obtained via EarthExplorer, USGS (<http://earthexplorer.usgs.gov>)



Ti, Al, Cr, Fe, Mn, Mg, Ca and Na; 40 s for Si, 100 s for F and 80 s for Cl. Values of  $\text{Fe}^{3+}$  were obtained following the formulation of Leake et al. (1997).

**Plagioclases** Compositional profiles (spacing  $\sim 4\text{--}8\ \mu\text{m}$ ) of major (Si, Al, Ca, Na and K) and minor (Ti, Fe, Mg, Sr and Ba) element concentrations were obtained in plagioclase phenocrysts. The analytical conditions consisted of an accelerating potential of 20 keV and electron beam current of 10 nA for major elements and 40 nA for minor elements with a defocused beam (2 to 5  $\mu\text{m}$ ) in order to reduce volatile alkali loss. Counting times for major elements were 32 s, 240 s for Ti, Fe and Ba, and 480 s for Mg and Sr.

**Clinopyroxenes and orthopyroxenes** Concentrations of major (Si, Mg, Fe and Ca), minor and trace (Ti, Al, Mn, Cr, Ni) elements were obtained in pyroxene phenocryst cores and rims. The analytical conditions consisted of an accelerating potential of 20 keV and electron beam current of 30 nA with a focused beam. Counting times for major elements were 60 s and 80 s for minor and trace elements. Values of  $\text{Fe}^{3+}$  were obtained following the formulation of Putirka (2008).

**Fe–Ti oxides** Compositional profiles (spacing  $\sim 2\text{--}3\ \mu\text{m}$ ) of major (Ti, Fe and O) and minor and trace (Al, Mg, Ca, Mn, V, Cr, Zn, Ni, Co and Si) elements were measured in titanomagnetite and ilmenite. The analytical conditions consisted of an accelerating potential of 15 keV and electron beam current of 30 nA with a focused beam. Counting times for all the elements were 60 s except for O, in which counting times were 260 s. Values of  $\text{Fe}^{3+}$  were obtained following the formulations of Droop (1987) for ilmenite grains and Stormer (1983) for titanomagnetites.

**Olivines** Concentrations of major (Si, Mg and Fe), minor and trace (Al, Ni, Mn, Ca) elements were obtained in the core of olivine phenocryst. Analyses were taken away from grain boundaries in order to avoid secondary fluorescence issues during the acquisition of Ca concentrations (cf. Dalton and Lane 1996). The analytical conditions consisted of an accelerating potential of 20 keV and electron beam current of 30 nA for Si, Fe, Mg and Mn and 100 nA for Al, Ni and Ca, all with a focused beam. Counting times for all the elements but Ca were 40 s and 400 s for Ca.

## Geothermobarometry

**Amphiboles** The methods of Ridolfi et al. (2010) and Ridolfi and Renzulli (2012) are used to calculate intensive conditions (T, P and  $f\text{O}_2$ ) independently in 109 amphibole cores from both Cal-149Ta (light-brown lapilli) and Cal-160 (white bomb) samples.

**Amphibole-plagioclases** The Holland and Blundy (1994) thermometry is applied using core compositions of 16 plagioclase-amphibole pairs, where equilibrium is assumed because the plagioclase crystals are found as inclusions in amphibole phenocrysts.

**Clinopyroxene-orthopyroxenes** Two-pyroxene thermobarometry (Putirka 2008) is used with 35 ortho- and clinopyroxene pairs that passed the test for equilibrium according to the Putirka (2008) chemical filter across the nine samples.

**Fe–Ti oxides** The Ghiorso and Evans (2008) thermoxybarometer is applied to compositions of crystal cores and close ( $\sim 2\ \mu\text{m}$  to the interface) to ilmenite-titanomagnetite grain boundaries.

**Olivine** The Ca-in-olivine thermometer of Shejwalkar and Coogan (2013) is applied to core composition data from 16 olivine phenocrysts in crystal clots, where equilibrium with the surrounding crystal phases (plagioclase, clinopyroxene and orthopyroxene) is assumed due to textural relation and chemical filters (cf. Grove et al. 1997). Nine calculated temperatures were discarded, due to the low forsterite content ( $\text{Fo}_{61\text{--}68}$ ) of the crystals considering  $\text{Fo}_{70}$  as the lower limit of the calibration of the thermometer (Shejwalkar and Coogan 2013).

The error propagation of geothermo- and geobarometers is carried out considering both internal uncertainties (associated with the experimental method) and external uncertainties (associated with precision and accuracy electron microprobe analyses). In later parts of this work, MELTS modelling uses the intensive physical variables derived from the thermobarometry (see ‘Intensive variable conditions’ section).

## Descriptions and compositions of the samples

According to Castruccio et al. (2016) the fall deposits of the 22–23 April eruptions are made up of four sub-units: the lower layer (unit 0) corresponds to the first event and is composed mainly of light-brown, highly vesicular basaltic andesite scoria and up to 10 vol.% of lithics. Layers 1, 2 and 3 correspond to the second (largest) event and there is a transition in the dominant clast type present in the deposits, from light-brown scoria in layer 1 to dark-brown, dense juveniles with the same composition within layer 3. Samples Cal-149Ta, Cal-155 and Cal-156 correspond to layer 1, the sample Cal-149Tb corresponds to layer 3, samples Cal-157, Cal-158 and Cal-159 correspond to scoriaceous bombs from PDCs, and sample Cal-160 corresponds to a distinctive, white bomb with darker zones extracted from a PDC deposit.

All samples are porphyric, with  $\sim 35$  to 65 vol.% of phenocrysts. Dominant mineral phases present in all the samples are plagioclase, orthopyroxene and clinopyroxene. Minor phases include amphibole (only in

Cal-149Ta and Cal-160), olivine (in all samples except Cal-160), titanomagnetite, ilmenite, apatite and chalcopyrite. All the mineral phases are present as clots of crystals and isolated crystals. The samples exhibit crystallinities of ~40 vol.% except for Cal-160, which shows a higher crystallinity of ~60 vol.% (Table 3). The samples show a large range of vesicularities: from 15 to 60 vol.% and the highest values correspond to light-brown lapilli (samples Cal-149Ta, Cal-155, Cal-156) from 42 to 60 vol.% (see details in Table 3). The crystallinity percentages and quantification of the main petrographic of the collected products of the April 2015 Calbuco eruption were obtained by image processing techniques via 'Background Extraction' of pseudo-coloured images through the freeware JMicrovision.

All the samples correspond to calc-alkaline basaltic-andesites (55.6–56.9 SiO<sub>2</sub> wt.%; Fig. 3a). The Mg# (Mg# = molar Mg/(Mg + Fe<sup>2+</sup>)) values are from 0.56 to 0.59. The maximum SiO<sub>2</sub> content (56.9 wt.%) and the minimum Mg# (0.56) correspond to the Sample Cal-160 (Table 4; Fig. 3). All samples show similar rare earth elements (REE) patterns, with a narrow range of La<sub>N</sub>/Yb<sub>N</sub> (2–2.4); only the sample Cal-155 shows a slight positive Eu anomaly (see Online Resource 1). The spider diagram of the studied samples shows similar trends in all samples and display positive Rb, Pb and Sr anomalies and negative Nb, P and Ti anomalies, which are typical of magmas from arc settings (Fig. 3c).

## Mineral chemistry and petrography

**Plagioclase** Plagioclase phenocrysts are 0.1–2.0 mm in size and can be found as isolated crystals and as members of cumulocrysts and glomerocrysts (together with pyroxene, olivine, titanomagnetite, apatite, amphibole and scarce sulphides). Most of the plagioclase phenocrysts display zonation patterns with distinct cores and rims, with the

exception of some crystals found as inclusions in amphibole and pyroxene crystals.

Two compositional types were identified in plagioclase phenocrysts: zone 1 corresponds to compositions of An<sub>80–92</sub> (Figs. 4 and 5), which is restricted to phenocryst cores. Zone 2 corresponds to compositions of An<sub>46–79</sub> (Fig. 4), mainly located on phenocryst rims, where oscillatory zonation is ubiquitous (Fig. 6). According to the presence/absence of these zones, plagioclase crystals have been classified into two groups:

- Group I: Crystal core shapes are euhedral to subhedral, resorption features and patchy zonation are not recognised. Core compositions correspond to zone 1 compositions. The rims have variable thickness (from 20 to 280 µm) and their compositions correspond to zone 2 compositions.
- Group II: These plagioclase crystals show oscillatory zoning within zone 2 compositional range. Resorption and sieve texture as well as patchy zoning are very common.

Plagioclase grains found as inclusions in amphibole have compositions in the range An<sub>50–89</sub>.

**Amphibole** Amphibole phenocrysts are found only in Cal-149Ta (fall deposit, layer 1) and Cal-160 (white bomb from PDC). All Cal-149Ta amphiboles of Cal-149Ta are pargasites (after Leake et al. 1997; Mg# = 0.64–0.74; Si apfu = 6.3–6.5; Fig. 7) and can be found as isolated crystals and glomerocrysts (together with plagioclase, pyroxene, titanomagnetite, olivine, ilmenite and apatite). All amphibole phenocrysts are euhedral and usually contain plagioclase inclusions. In sample Cal-160, 70% of the amphiboles are edenite (NaCa<sub>2</sub>Mg<sub>5</sub>(AlSi<sub>7</sub>)O<sub>22</sub>(OH)<sub>2</sub>) (after Leake et al. 1997; Mg# = 0.65–0.77; Si apfu = 6.5–6.6; Fig. 8), and 30% are pargasites (NaCa<sub>2</sub>(Mg,Fe)<sub>4</sub>Al(Al<sub>2</sub>Si<sub>6</sub>)O<sub>22</sub>(OH)<sub>2</sub>) (after

**Table 3** Main features of the samples analysed from Calbuco's April 2015 eruption

Section name (Cal-)	149Ta	149Tb	155	156	157a	157b	158	159	160
Description	LL	DL	LL	LL	DB	DB	DB	DB	WB
Vesicles (total %)	59.8	15.4	42.3	51.4	32.9	49.7	41.1	37.2	25.4
Groundmass (total %)	22.3	52.9	38	31.5	37	28.9	35.8	39.6	27.1
Plagioclases (total %)	12	23.1	14.7	12.9	18.1	14.2	16.1	15.7	35.2
Pyroxenes (total %)	3.8	7.1	3.7	3.9	11.1	5.8	5.4	6.3	9.7
Amphiboles (total %)	1.2	–	–	–	–	–	–	>0.1	>0.1
Olivine (total %)	–	0.1	0.1	>0.1	0.1	>0.1	0.1	>0.1	–
Oxides (total%)	0.9	1.4	1.2	0.3	0.9	1.4	1.5	1.2	2.5
Crystallinity (%) <sup>a</sup>	44.5	37.5	34.1	35.2	44.9	42.5	39.2	36.9	63.7

LL light-brown lapilli, DL dark lapilli, DB dark bomb, WB white bomb

<sup>a</sup> Percentage not considering vesicles



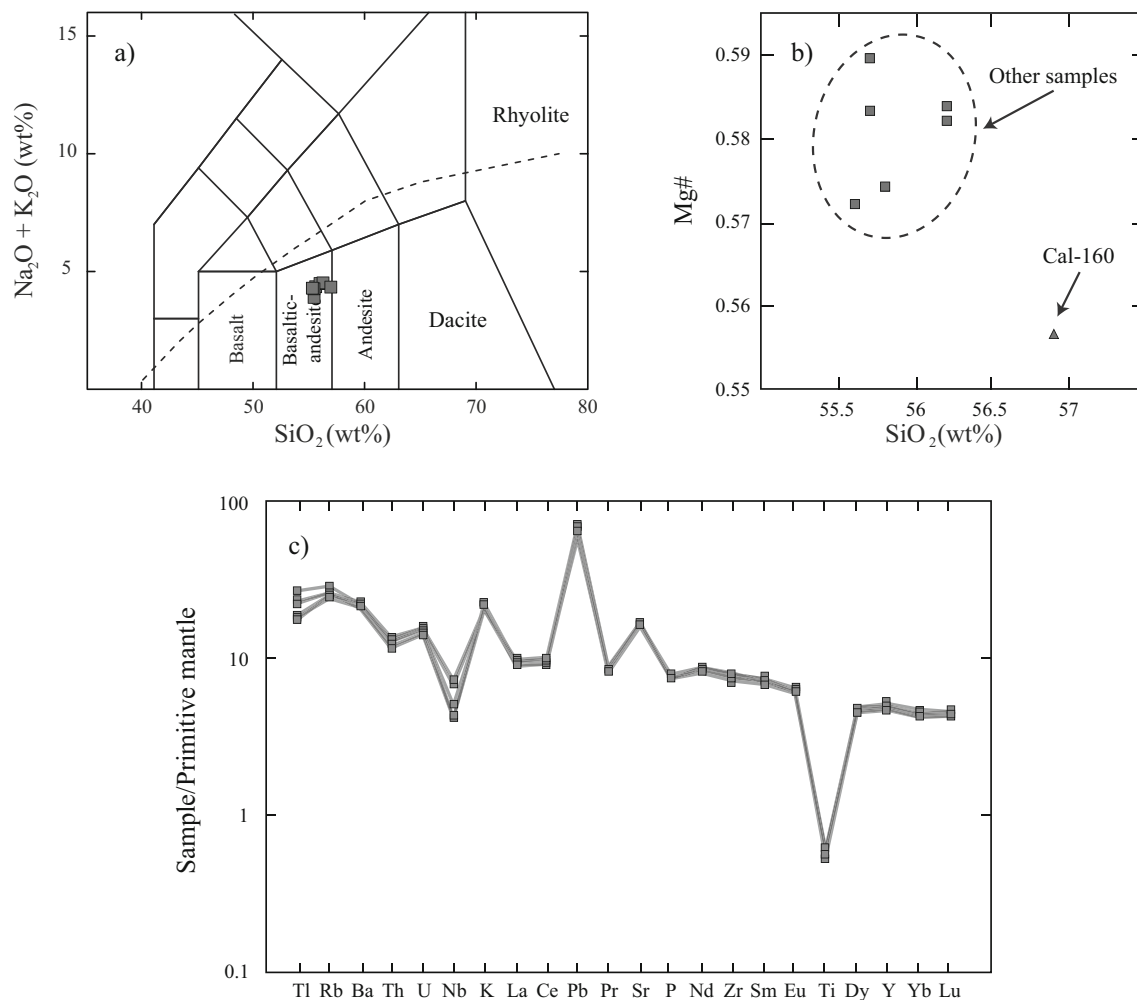


**Fig. 3** (a) Total alkali versus silica (Le Bas et al. 1986) plots of the Calbuco 2015 volcanic products. Boundary dashed line between alkaline and subalkaline rocks is taken from Irvine and Baragar (1971). (b) Variation diagram of  $\text{SiO}_2$  (wt.%) versus Mg# (details in Table 4), where

sample Cal-160 shows the highest Mg# and the lowest  $\text{SiO}_2$  wt.%. (c) Primitive mantle-normalised (Sun and McDonough 1989) spider diagram. Details of major and trace element concentrations are available in Table 4

Leake et al. 1997;  $\text{Mg\#} = 0.71\text{--}0.77$ ;  $\text{Si apfu} = 6.2\text{--}6.5$ ). In contrast to Cal-149Ta, amphiboles in Cal-160 are anhedral and are found as members of glomerocrysts (together with plagioclase, pyroxene, titanomagnetite, olivine, ilmenite and apatite).

**Fe–Ti oxides** Ilmenite grains are scarce and have composition of  $X_{\text{ilm}}$  (i.e. the cation atomic proportion of Ti) =  $0.77\text{--}0.85$  (i.e.  $X_{\text{hmt}}$ , the cationic proportion of  $\text{Fe}^{2+}$  =  $0.15\text{--}0.23$ ). They occur as both inclusions and in contact with titanomagnetites. Titanomagnetites can be classified into two groups: high-Ti, with a relatively high ulvöspinel component ( $X_{\text{usp}} = 0.42\text{--}0.46$ ;  $X_{\text{mgt}} = 0.54\text{--}0.58$ ) and low-Ti ( $X_{\text{usp}} = 0.10\text{--}0.17$ ;  $X_{\text{mgt}} = 0.83\text{--}0.9$ ). They appear as isolated crystals or in clots of crystals together with amphibole, plagioclase, pyroxene, olivine, ilmenite and apatite.

**Pyroxenes** Pyroxenes are found both as isolated grains and as members of clots of crystals together with amphibole, plagioclase, pyroxene, olivine, ilmenite, titanomagnetite, apatite and chalcopryrite (see Online Resource 2). All the pyroxene crystals exhibit slight reverse and oscillatory zoning. Clinopyroxene crystals exhibit reverse zoning, from  $\text{En}_{43\text{--}47}\text{Fe}_{9\text{--}15}\text{Wo}_{40\text{--}44}$  (Fig. 8) composition in the cores to  $\text{En}_{44\text{--}46}\text{Fe}_{10\text{--}12}\text{Wo}_{43\text{--}45}$  composition in the rims (Figs. 8 and 9); oscillatory zoning with compositions of  $\text{En}_{43\text{--}46}\text{Fe}_{10\text{--}13}\text{Wo}_{42\text{--}45}$  (Figs. 8 and 9) have also been observed. Orthopyroxenes exhibit reverse zoning from  $\text{En}_{67\text{--}69}\text{Fe}_{29\text{--}31}\text{Wo}_{2\text{--}3}$  composition in the cores to  $\text{En}_{69\text{--}71}\text{Fe}_{26\text{--}28}\text{Wo}_{2\text{--}3}$  composition in the rims (Fig. 9); oscillatory zoning with compositions of  $\text{En}_{69\text{--}72}\text{Fe}_{24\text{--}27}\text{Wo}_{2\text{--}4}$  (Figs. 8 and 9) have also been recognised.

**Table 4** Whole-rock analyses of samples from the 2015 Calbuco eruption

	Detection limit	Cal-149A Lapilli	Cal-149B Lapilli	Cal-155 Lapilli	Cal-157 Bomb	Cal-158 Bomb	Cal-159 Bomb	Cal-160 Bomb
SiO <sub>2</sub>	0.01 (%)	56.2	56.2	55.6	55.7	55.8	55.7	56.9
Al <sub>2</sub> O <sub>3</sub>	0.01 (%)	18.8	18.7	18.9	18.8	18.9	18.7	18.6
TiO <sub>2</sub>	0.01 (%)	0.93	0.92	0.87	0.92	0.93	0.94	0.82
FeO	0.2 (%)	4.99	4.99	5.69	5.27	5.55	5.27	5.41
Fe <sub>2</sub> O <sub>3</sub>	0.01 (%)	2.87	2.77	2.22	2.60	2.41	2.71	2.17
MnO	0.01 (%)	0.16	0.16	0.17	0.17	0.17	0.15	0.16
MgO	0.01 (%)	3.93	3.9	4.27	4.14	4.2	4.25	3.81
CaO	0.01 (%)	8.04	7.96	8.21	8.16	8.14	8.12	7.63
Na <sub>2</sub> O	0.01 (%)	3.77	3.78	3.45	3.65	3.65	3.65	3.67
K <sub>2</sub> O	0.01 (%)	0.62	0.64	0.53	0.61	0.61	0.61	0.67
P <sub>2</sub> O <sub>5</sub>	0.01 (%)	0.17	0.16	0.15	0.16	0.16	0.16	0.16
LOI		−0.3	−0.3	−0.2	−0.3	−0.3	−0.3	−0.1
Total		100.48	100.18	100.06	100.18	100.52	100.26	99.99
Li	0.03 (ppm)	15.12	15.65	14.85	14.83	14.17	14.69	16.87
Sc	0.05 (ppm)	21.75	22.82	21.43	23.23	22.76	24.04	19.91
V	0.07 (ppm)	181.7	183.7	185.3	189.3	188.6	197.1	170.1
Co	0.01 (ppm)	40.90	38.86	43.27	38.36	38.29	34.86	34.81
Ni	0.32 (ppm)	10.01	10.81	11.73	12.92	15.72	12.88	11.00
Cu	0.66 (ppm)	44.19	45.37	24.05	50.56	47.50	45.99	36.92
Cr	0.01 (ppm)	12.90	14.92	15.08	18.19	17.41	16.98	15.84
Zn	2.207 (ppm)	79.84	75.96	79.41	76.31	78.27	81.24	81.82
Tl	0.04 (ppm)	0.115	0.111	0.117	0.094	0.091	0.088	0.135
Rb	0.01 (ppm)	16.48	16.37	14.27	15.92	15.17	15.83	18.35
Ba	0.5 (ppm)	152.1	151.6	131.4	146.0	139.7	145.3	164.0
Th	0.001 (ppm)	1.10	1.03	0.88	1.02	0.97	1.01	1.20
U	0.001 (ppm)	0.310	0.310	0.259	0.304	0.287	0.296	0.350
Nb	0.003 (ppm)	152.09	151.65	131.44	145.98	139.66	145.29	164.03
La	0.001 (ppm)	1.098	1.028	0.882	1.020	0.971	1.010	1.201
Ce	0.002 (ppm)	0.31	0.31	0.26	0.30	0.29	0.30	0.35
Pb	0.14 (ppm)	4.99	4.67	6.57	4.02	4.25	4.39	4.96
Pr	0.005 (ppm)	2.391	2.411	1.950	2.301	2.194	2.287	2.450
Sr	0.02 (ppm)	347	355	375	350	335	352	353
Nd	0.001 (ppm)	11.79	11.82	9.44	11.35	10.80	11.27	11.81
Zr	0.06 (ppm)	88.50	87.26	68.32	83.80	79.55	83.97	89.78
Sm	0.001 (ppm)	3.271	3.259	2.478	3.143	3.012	3.155	3.111
Eu	0.001 (ppm)	1.030	1.083	0.957	1.019	0.993	1.003	1.026
Gd	0.001 (ppm)	3.520	3.453	2.626	3.355	3.225	3.369	3.278
Tb	0.001 (ppm)	0.583	0.584	0.436	0.562	0.546	0.571	0.546
Dy	0.001 (ppm)	3.576	3.577	2.648	3.439	3.308	3.452	3.338
Ho	0.001 (ppm)	0.784	0.776	0.581	0.752	0.723	0.756	0.726
Er	0.01 (ppm)	2.221	2.204	1.651	2.121	2.047	2.131	2.062
Y	0.01 (ppm)	22.48	23.16	17.13	22.06	20.90	22.18	21.27
Yb	0.01 (ppm)	2.187	2.300	1.719	2.171	2.056	2.114	2.047
Lu	0.002 (ppm)	0.333	0.335	0.254	0.322	0.311	0.326	0.316

**Olivine** Olivine grains are found surrounded by pyroxene and titanomagnetite crystals (see example images on Online Resource 2). Their composition of Fo<sub>60–75</sub> (Fig. 8) is fairly homogeneous for each crystal, thus no zonation patterns are recognised. Olivine crystals were found in all the samples except Cal-160 (Table 3).

## Intensive variable conditions

### Two-pyroxene thermobarometry

Mineral pairs measured in all samples except Cal-160 give temperatures of 958–1013 ± 56 °C (Fig. 10; Table 5), with

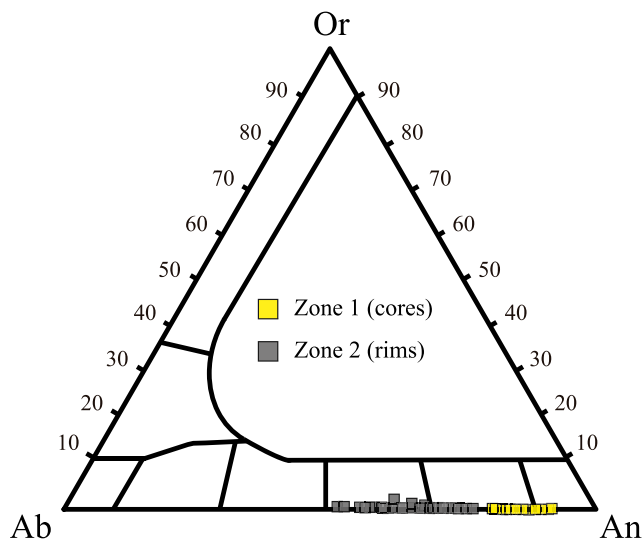


**Figure. 4** Plagioclase compositions of the studied samples. Zone 1 represents core compositions of group I, whereas zone 2 represents rim compositions of group I and the whole-crystal composition of group II

an average of  $984 \pm 12 \text{ }^{\circ}\text{C}$ , and pressures of  $1.5\text{--}4.7 \pm 3.2 \text{ kbar}$  (Table 5), with an average of  $3.3 \text{ kbar}$  ( $\sigma = 0.8 \text{ kbar}$ ). The pairs measured in the sample Cal-160 give temperatures of  $944\text{--}981 \pm 56 \text{ }^{\circ}\text{C}$  (Fig. 10; Table 6), with an average of  $968 \pm 13 \text{ }^{\circ}\text{C}$ , and pressures of  $3.9\text{--}6.8 \pm 3.2 \text{ kbar}$  (Table 6), with an average pressure of  $5.7 \text{ kbar}$  ( $\sigma = 1.3 \text{ kbar}$ ).

### Amphibole thermobarometry and oxybarometry

Sample Cal-149Ta (light-brown lapilli): The thermometer of Ridolfi et al. (2010) gives temperatures of  $894\text{--}922 \pm 24 \text{ }^{\circ}\text{C}$  (Fig. 10; Table 5), with an average temperature of  $906 \pm 7 \text{ }^{\circ}\text{C}$ , a range and average which is slightly lower than those obtained by two-pyroxene thermometry. The pressure conditions obtained using the Ridolfi et al. (2010) barometer are  $2\text{--}2.6 \pm 0.3 \text{ kbar}$  (Fig. 11; Table 5), with an average pressure of  $2.3 \text{ kbar}$  ( $\sigma = 0.1$ ). The relative oxygen fugacity values given by the Ridolfi et al. (2010) oxygen barometer are between 0.2

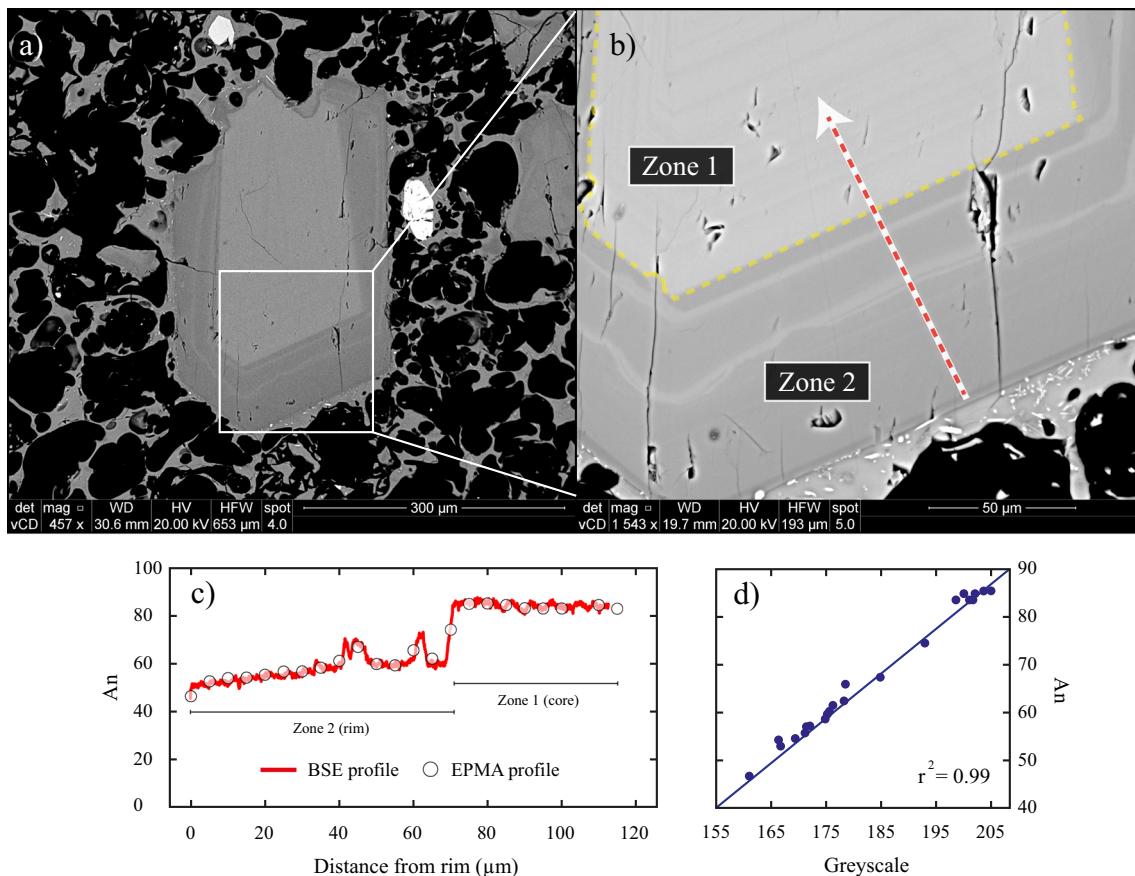


**Figure 5** (a) Backscatter electron (BSE) image of a plagioclase crystal representative of group I. Brighter greyscale colours are correlated to higher density. (b) The arrow represents the profile measured by electron microprobe (EPMA) and its direction. (c) Anorthite profile composition ( $An = 100 \times Ca/(Ca + Na + K)$ ; elements in moles) by EPMA of the measured profile (circles) coupled with the n (BSE) profile based on greyscale values calibrated with the composition measured by electron microprobe

(solid line). (d) Relation and coefficient of determination ( $r^2$ ) between BSE profile and the measured anorthite content (An). Group I plagioclases have compositions corresponding to zone 1 ( $An_{80\text{--}92}$ ) in the core and zone 2 ( $An_{46\text{--}79}$ ) in the rims. 'An' represents the composition of plagioclases because in all crystals the K content is fairly constant (see Fig. 4)

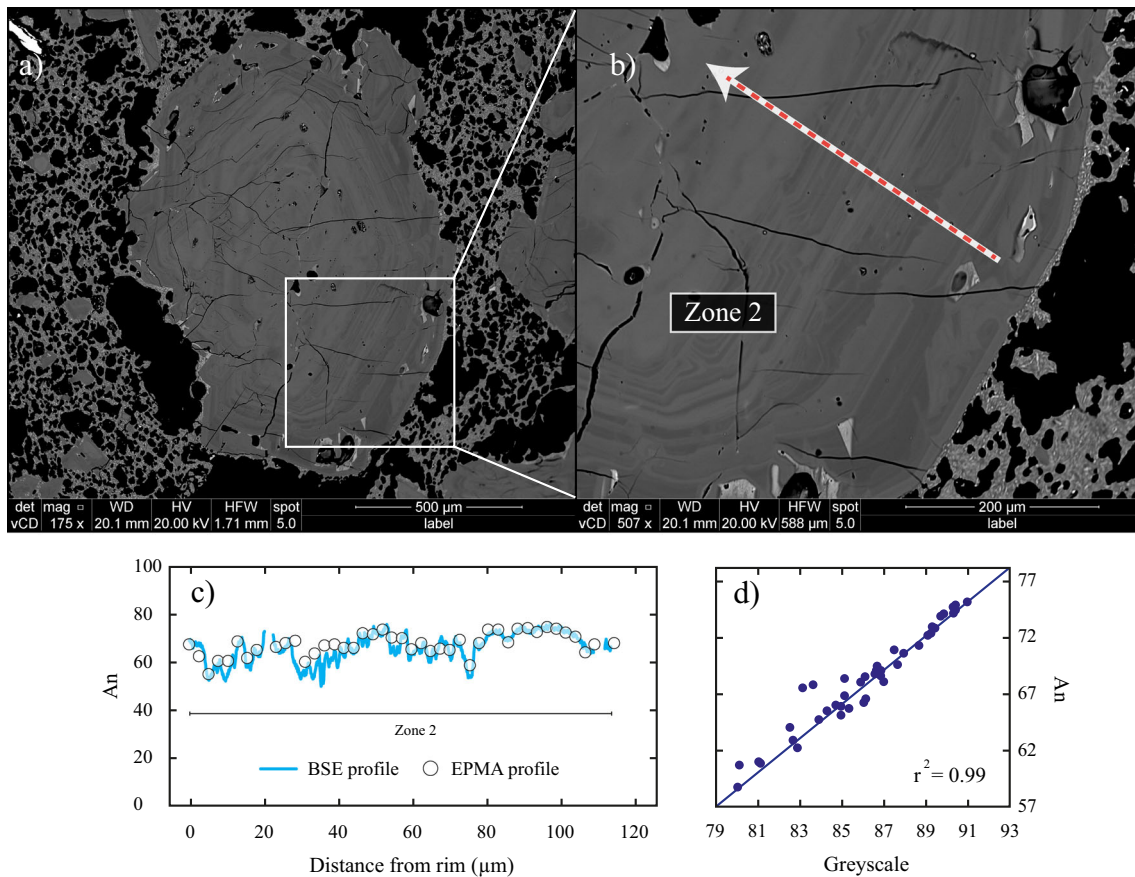


**Figure 6** (a) Backscatter electron (BSE) image of a plagioclase crystal representative of group II. Brighter greyscale colours are correlated to higher density. (b) The arrow represents the profile measured by electron microprobe (EPMA) and its direction. Anorthite profile composition ( $An = 100 \times Ca/(Ca + Na + K)$ ; elements in moles) by EPMA of the measured profile (circles) coupled with the backscatter electron (BSE) profile

based on greyscale values calibrated with the composition measured by electron microprobe (solid line). (d) Relation and coefficient of determination ( $r^2$ ) between BSE profile and the measured anorthite content (An). Group II plagioclases have compositions corresponding to zone 2 ( $An_{46-79}$ ). 'An' is representing the composition of plagioclases because in all crystals the K content is fairly constant (see Fig. 4)

and  $0.5 (\pm 0.4) \Delta NNO$  units (Table 5), with an average of  $0.3 \Delta NNO$  ( $\sigma = 0.1$ ). The Ridolfi and Renzulli (2012)

thermometer yields temperatures of  $882-910 \pm 16$  °C (Fig. 10; Table 5), with an average temperature of 897 °C

**Figure 7** Amphibole compositions and classification (after Leake et al. 1997) of samples Cal-149Ta (grey circles) and Cal-160 (dark circles). All amphiboles of the sample Cal-149Ta correspond to pargasites, whereas amphiboles of sample Cal-160 correspond to 70% edenites and 30% pargasites

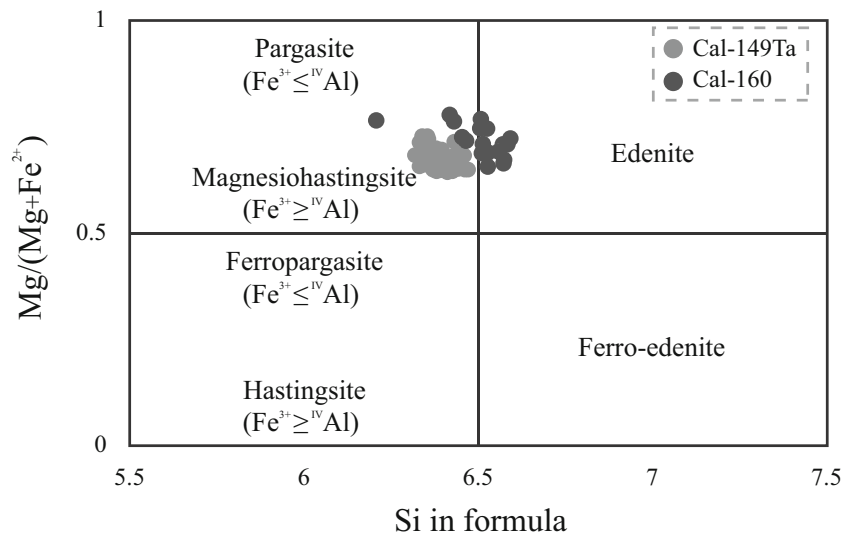
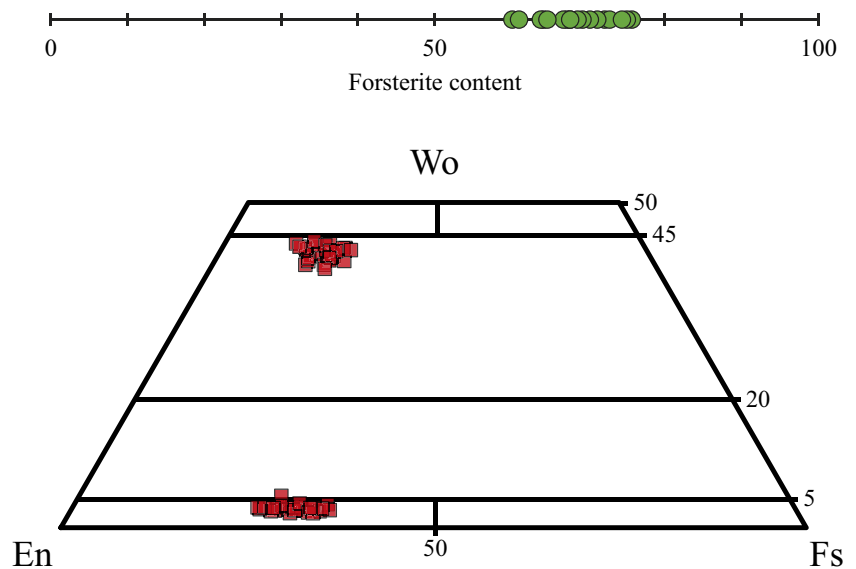




**Figure 8** Olivine (found in all samples except Cal-160) and pyroxene (clino- and orthopyroxene, found in all samples, including Cal-160) compositions of the analysed samples



( $\sigma = 7^\circ\text{C}$ ). For the same amphiboles, pressures of  $1.9\text{--}2.3 \pm 0.4$  kbar (Fig. 11; Table 5), with an average of 2.1 kbar ( $\sigma = 0.1$  kbar), are obtained. The relative oxygen fugacities given by the Ridolfi and Renzulli (2012) oxygen barometer are between  $-0.9$  and  $-0.2$   $\Delta\text{NNO}$  (Table 5), with an average of  $-0.6$   $\Delta\text{NNO}$  ( $\sigma = 0.1$ ).

Sample *Cal-160* (white bomb): Temperatures obtained by the thermometer of Ridolfi et al. (2010) are  $862\text{--}886 \pm 23^\circ\text{C}$  (Fig. 10; Table 6), similar to Cal-149Ta amphibole temperatures, with an average of  $874^\circ\text{C}$  ( $\sigma = 7^\circ\text{C}$ ). The Ridolfi et al. (2010) barometer gave pressures between 1.6 and  $2 \pm 0.3$  kbar (Fig. 11; Table 6) and an average pressure of 1.8 kbar ( $\sigma = 0.2$  kbar). The relative oxygen fugacity values are between 0.2 and  $0.5 \pm 0.4$   $\Delta\text{NNO}$  (Ridolfi et al. 2010; Table 6), with an average of 0.3  $\Delta\text{NNO}$  ( $\sigma = 0.1$ ). The Ridolfi and Renzulli (2012) thermometer gives temperatures of  $823\text{--}859 \pm 23^\circ\text{C}$  (Fig. 10; Table 6) with an average of  $842^\circ\text{C}$  ( $\sigma = 11^\circ\text{C}$ ). The same amphiboles gave pressures of  $1.4\text{--}1.8 \pm 0.4$  kbar (Fig. 11; Table 6), with an average pressure of 1.6 kbar ( $\sigma = 0.1$  kbar). According to the oxygen barometer of Ridolfi and Renzulli (2012), oxygen fugacity is between 0.4 and 0.8  $\Delta\text{NNO}$  (Table 6), with an average of 0.7  $\Delta\text{NNO}$  ( $\sigma = 0.1$ ).

### Plagioclase-amphibole thermometry

Twelve pairs of amphibole-plagioclase in sample Cal-149Ta give equilibrium temperatures of  $945\text{--}1018 \pm 42^\circ\text{C}$  (Fig. 10; Table 5), with an average temperature of  $977^\circ\text{C}$  ( $\sigma = 26^\circ\text{C}$ ). Sample Cal-160 gives lower equilibrium temperatures of  $902\text{--}934 \pm 42^\circ\text{C}$  (Fig. 10; Table 6) with an average temperature of  $914^\circ\text{C}$  ( $\sigma = 18^\circ\text{C}$ ). All these temperatures are higher than those obtained by the methods of Ridolfi et al. (2010) and Ridolfi and Renzulli (2012) based on single amphibole compositions.

### Ilmenite–titanomagnetite thermometry and oxygen barometry

Ilmenite–titanomagnetite pairs are found only in samples Cal-149Tb (very scarcely), Cal-155 (very scarcely) and Cal-160 (common), and give temperature and oxygen fugacity values which all fell within the calibrated temperature and oxygen fugacity ranges of 800 to  $1300^\circ\text{C}$ , and  $-3$  to  $+3$  log units  $\Delta\text{NNO}$ , respectively. The core compositions gave large ranges of both temperature ( $841\text{--}966 \pm 22^\circ\text{C}$ ; Fig. 10) and oxygen fugacity ( $0.2\text{--}0.75 \pm 0.9$   $\Delta\text{NNO}$ ; Table 7); the rims give significantly different intensive conditions only in the sample Cal-160, with calculated temperatures ranging from 900 to  $1073^\circ\text{C}$  (Fig. 10) and oxygen fugacities from 0.2 to  $0.75 \pm 0.1$   $\Delta\text{NNO}$  (Table 7). Details of intensive conditions related to each ilmenite–titanomagnetite pair and associated errors are given below and included in Table 7.

Samples *Cal-149Tb* and *Cal-155*: Temperatures are calculated from four core compositions of ilmenites and associated titanomagnetites considering diverse measurements (details in Online Resource 3). Individual pairs of grains show fairly constant compositions and, consequently, similar temperatures and oxygen fugacities, but different temperatures are obtained in different samples (see Table 7). For the sample Cal-149Tb, the temperatures are  $961\text{--}1008 \pm 22^\circ\text{C}$  (average  $982^\circ\text{C}$ ,  $\sigma = 23^\circ\text{C}$ ) and oxygen fugacities are 0.36–0.45  $\Delta\text{NNO}$  (average 0.41  $\Delta\text{NNO}$ ,  $\sigma = 0.04$ ); for sample Cal-155, temperatures are  $902\text{--}922 \pm 22^\circ\text{C}$  (average  $907^\circ\text{C}$ ,  $\sigma = 10^\circ\text{C}$ ) and oxygen fugacities are 0.17–0.23  $\Delta\text{NNO}$  (average 0.2  $\Delta\text{NNO}$ ,  $\sigma = 0.13$ ).

Sample *Cal-160*: In every crystal pair, compositions close to the boundary between these two mineral phases

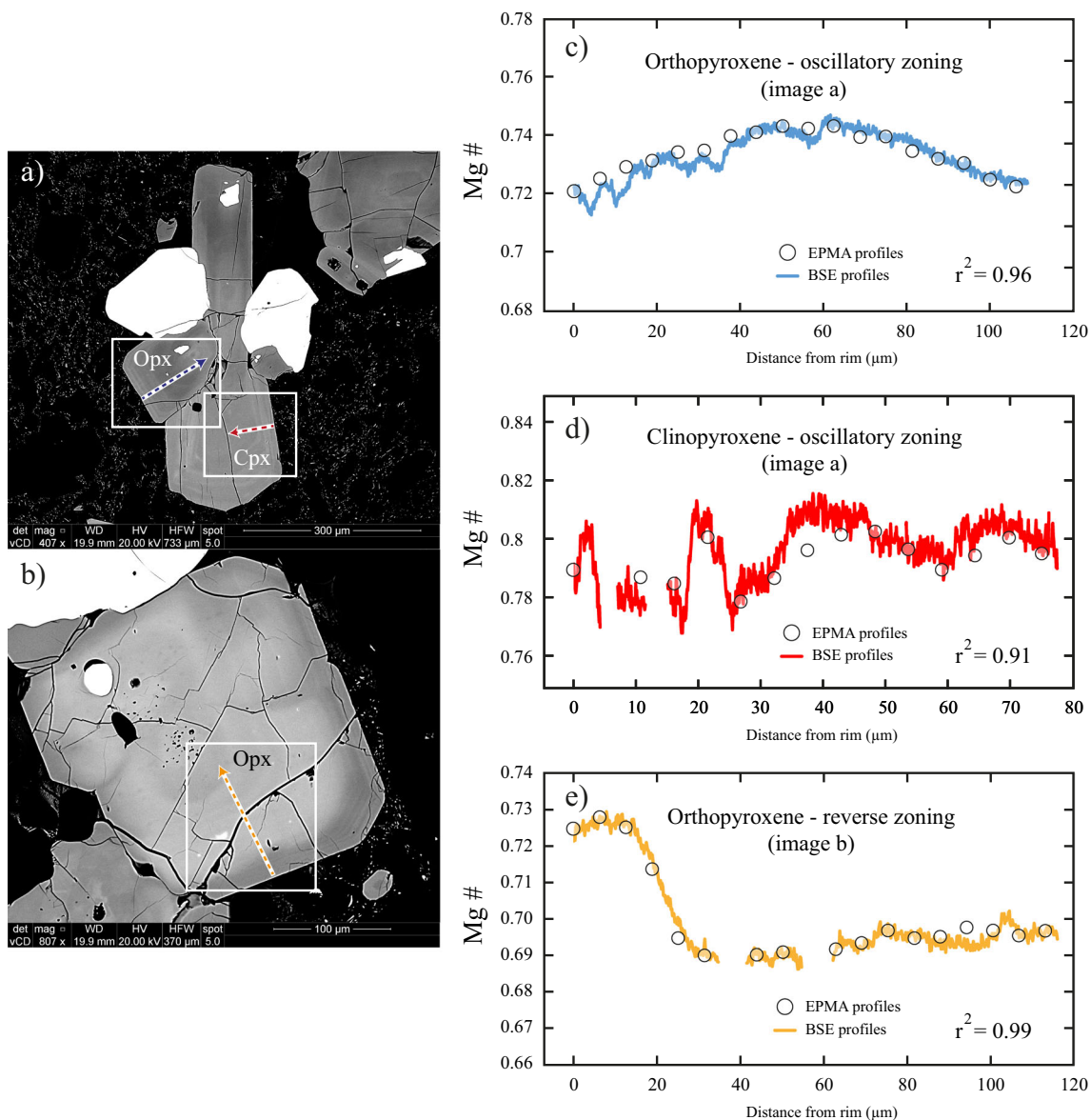


**Figure 9** (a, b) Backscatter electron (BSE) images of clots of crystals where representative pyroxenes with oscillatory and reverse zonation patterns are found. Brighter greyscale colours are correlated to higher density. Arrows represent the measured profiles by electron microprobe (EPMA) and their directions. The orthopyroxene profile in (a) is shown in (c) and the clinopyroxene profile in (a) is shown in (d). The orthopyroxene profile in (b) is shown in (e). (c, d, e) Mg# ( $\text{Mg\#} = \text{Mg}/(\text{Mg} + \text{Fe}^{2+})$ ; elements in moles) of the measured profile (circles) coupled

with the backscatter electron (BSE) profile based on greyscale values calibrated with the composition measured by EPMA (solid line). The relation and coefficient of determination ( $r^2$ ) between BSE profile and the Mg# measured content. Greyscale values represent Mg# because the content of Ca within pyroxene crystals is fairly constant. Mg# represents the composition of pyroxenes because in all crystals the Ca content is fairly constant (see Fig. 8)

give considerably higher temperatures and slightly lower oxygen fugacity than core compositions (see Table 7). Cal-160 core temperatures are  $841\text{--}894 \pm 17$  °C (average 870 °C,  $\sigma = 18$  °C) with oxygen fugacities of  $0.5\text{--}0.94 \pm 0.09$   $\Delta\text{NNO}$  (average 0.64  $\Delta\text{NNO}$ ,  $\sigma = 0.18$ ), whereas rim temperatures are  $947\text{--}1073 \pm 23$  °C (average 1018 °C,  $\sigma = 45$  °C) and oxygen fugacities are  $0.21\text{--}0.75 \pm 0.09$   $\Delta\text{NNO}$  (average 0.48  $\Delta\text{NNO}$ ,  $\sigma = 0.16$ ).

### Ca-in-olivine thermometry

Seven olivine cores give temperatures of  $987\text{--}1019 \pm 22$  °C (Fig. 10; Table 5), with an average temperature of 997 °C ( $\sigma = 13$  °C). These Ca-in-olivine temperatures are therefore consistent with those obtained using the two-pyroxenes, Fe-Ti oxides and plagioclase-amphibole thermometers for the same samples.

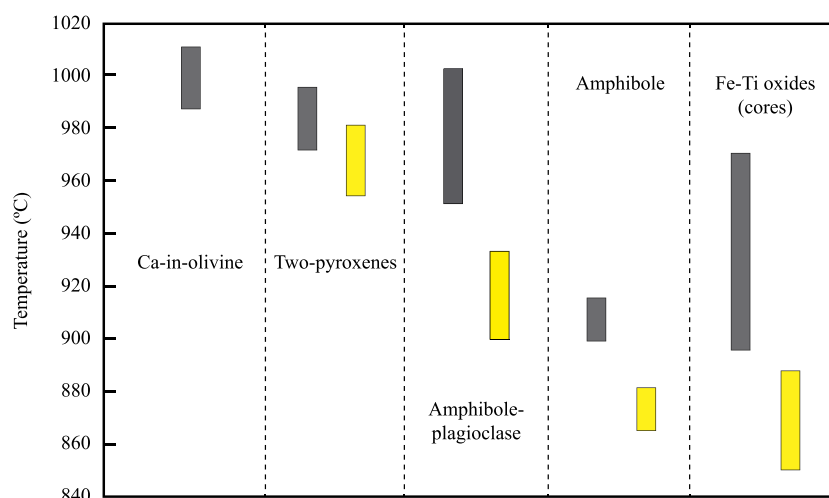


**Fig. 10** Diagram showing the results of several thermometers (Ca-in-olivine, Shejwalkar and Coogan 2013; two-pyroxenes, Brey and Köhler 1990; Putirka 2008; amphibole-plagioclase, Holland and Blundy 1994; amphibole, Ridolfi and Renzulli 2012; Fe–Ti oxides (cores), Ghiorso and Evans 2008). Vertical bars represent values of average temperature  $\pm$  one

standard deviation of all the samples except Cal-160 (grey) and Cal-160 (yellow). Sample Cal-160 gave temperatures systematically lower than the others. Ca-in-olivine was not used in sample Cal-160 because olivine was not found

## MELTS modelling

The initial melt composition used in MELTS (Ghiorso and Sack 1995) modelling corresponds to the anhydrous ground-mass composition of sample Cal-159 (Table 4) because it shows the highest Mg# (0.59), and possesses representative mineral assemblages and textural features observed in all April 2015 Calbuco products. The initial composition is calculated via an extraction of the modal composition of representative mineral phases from the whole-rock composition of the sample (Table 3). Details of the MELTS modelling results are available as Online Resource 4.

Zone 2 compositions of plagioclase phenocrysts (later rims and crystals) and the entire range of observed clinopyroxene and orthopyroxene compositions are reproduced by MELTS at conditions of 2–4% dissolved water, 2–6 kbar of pressure, temperatures from 900 to 1060 °C and crystallinity of 16–35 wt.%. Conversely, the zone 1 composition of older plagioclase phenocryst cores and the remaining phases (notably amphibole, olivine and Fe–Ti oxides) are not reproduced.

Crystallisation modelling of the products gives a range of solid phases between 16 and 35 wt.%. This range does not consider other mineral phases that could not be reproduced by MELTS (amphibole, olivine, ilmenite, titanomagnetite and zone 1 of plagioclase phenocrysts), which increases the crystallinity considerably (see details in Online Resource 4).

## Discussion

All the April 2015 Calbuco samples studied here (including sample Cal-160) have characteristics typical of Calbuco's products documented previously for all the volcanic units by López-Escobar et al. (1995b), Moreno et al. (2006), Sellés and Moreno (2011) and Daga et al. (2014). These include whole-rock chemistry, mineral assemblage and textural features (cf. Tables 1 and 2). Additionally, the trace-element data (Fig. 3c) show no significant differences in either elemental concentrations or distribution patterns across the whole sample suite (including Cal-160). Of the whole-rock chemistry of the April 2015 Calbuco

**Table 5** Calculated intensive conditions, methods and associated errors of the samples except Cal-160

Method	References	$T$ (°C)	Error (±)	Average (°C)	SD (σ)	$P$ (kbar)	Error (±)	Average (kbar)	SD (σ)	$fO_2$ $\Delta NNO$	Error (±)
Two-pyroxenes	Putirka (2008)	958–1013	56	984	12	1.5–4.7	3.2	3.3	0.8	–	–
Amphibole	Ridolfi et al. (2010)	894–922	24	906	7	2–2.6	0.3	2.3	0.1	0.2–0.5	0.4
	Ridolfi and Renzulli (2012)	882–910	16	897	7	1.9–2.3	0.4	2.1	0.1	–0.9–0.2	–
Plagioclase-amphibole	Holland and Blundy (1994)	945–1018	42	977	26	–	–	–	–	–	–
Ca-in-olivine	Shejwalkar and Coogan (2013)	987–1019	22	997	13	–	–	–	–	–	–

**Table 6** Calculated intensive conditions, methods, and associated errors of the sample Cal-160

Method	References	T (°C)	error (±)	Average (°C)	Std. Dev. (σ)	P (kbar)	error (±)	Average (kbar)	Std. Dev. (σ)	$fO_2$ ΔNNO	error (±)
Two-pyroxenes	Putirka (2008)	944–981	56	968	13	3.9–6.8	3.2	5.7	1.3	—	—
Amphibole	Ridolfi et al. (2010)	862–886	23	874	7	1.6–2.0	0.3	1.8	0.2	0.2–0.5	0.4
	Ridolfi and Renzulli (2012)	823–859	23	842	11	1.4–1.8	0.4	1.6	0.1	0.4–0.8	—
Plagioclase-amphibole	Holland and Blundy (1994)	902–934	42	914	18	—	—	—	—	—	—

eruption presented here (55.6–56.9 wt.% SiO<sub>2</sub>), the compositions are very similar to those reported for this eruption by Castruccio et al. (2016) for scoriaceous, pumiceous and dense juvenile products (54.5–58.1 wt.% SiO<sub>2</sub>). Further, the composition of the products analysed here are chemically within the

range of older units (unit 1—50.5–60.3 wt.% SiO<sub>2</sub>, unit 2—57.1–61 wt.% SiO<sub>2</sub>, unit 3—54.3–64.5 wt.% SiO<sub>2</sub>; López-Escobar et al. 1995b; Sellés and Moreno 2011) and other deposits of unit 4 (54.8–58.6 wt.% SiO<sub>2</sub>; López-Escobar et al. 1995b). The mineral assemblage has been fairly constant during the history of the volcano (Sellés and Moreno 2011), it being composed of plagioclase, clinopyroxene, orthopyroxene, amphibole, ilmenite, titanomagnetite and olivine (see Table 1), the latter always being surrounded by pyroxenes, plagioclase and Fe–Ti oxides.

### Mush reservoir in the upper crust

The Calbuco volcanic products of 2015 possess several features that have been regarded as consistent with mush-zone magma storage, in the manner proposed by, for example, Hildreth (2004) and Bachmann and Bergantz (2006). These features include high crystallinity (~40–60 vol.%) of the volcanic products (cf. Hildreth 2004; Bachmann and Bergantz 2006), the presence of clots of crystals where interstitial glasses are locally well preserved and compositionally different from the outer glasses (e.g. Saunders et al. 2010; Passmore et al. 2012; Spera and Bohrsen 2018) and the presence of complex textural features that suggest episodes of re-equilibration (cf. Moore et al. 2014). Although only small compositional ranges are recognised here for Calbuco in plagioclase, pyroxene and amphibole, the complex mineralogical textures commonly observed indicate a prolonged history of crystallisation and with changes in either temperature, pressure, melt composition, oxygen fugacity or other intensive variables through a protracted period of time (see Figs. 5, 6 and 9).

Our assumption that at the Cal-159 groundmass is a reasonable proxy for the melt composition in equilibrium with the crystal mush is supported by the MELTS modelling which can reproduce the compositions of the dominant crystal phases of plagioclase (zone 2), ortho- and clino-pyroxene. Pressure ranges obtained via amphibole barometry (considering average and standard deviation pressures) suggest the location of the mush reservoir at shallow depth. The barometer calibrated by Ridolfi et al. (2010) gives pressures equivalent to

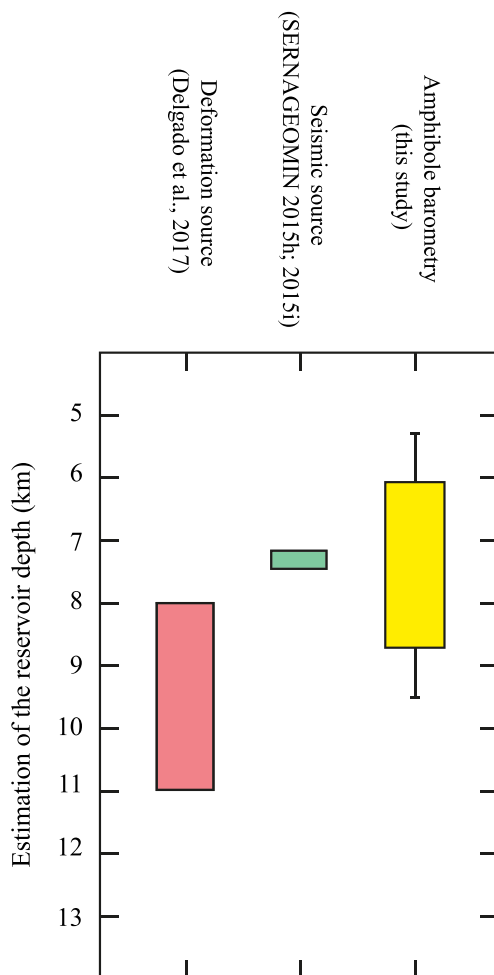


**Fig. 11** Comparison of different methods that allow the estimation of the reservoir depth: amphibole barometry (yellow bar and including errors; this study), seismic source (green bar; SERNAGEOMIN 2015h, 2015i) and deformation source (red bar; Delgado et al. 2017). The full barometry depth range is from 5.5 to 11 km (considering different pressure condition approaches) and corresponds to upper-to-middle crust conditions



**Table 7** Fe–Ti oxide core (pre-heating) and rim (during heating) intensive conditions rank ordered by core temperature

Sample	Pair	Place	$T$ (°C)	SD	Error	$fO_2$ ( $\Delta NNO$ )	SD	Error	Place	$T$ (°C)	Error	$fO_2$ ( $\Delta NNO$ )	Error
160	Fig1_p2	Core	841	6	12	0.94	0.05	0.04	Rim	1041	14	0.55	0.04
160	Fig1_p1	Core	841	7	12	0.91	0.03	0.04	Rim	1067	17	0.5	0.05
160	Fig1_p3	Core	846	4	12	0.9	0.02	0.04	Rim	1005	15	0.56	0.05
160	Fig1_p1	Core	865	8	15	0.5	0.06	0.09	Rim	1068	15	0.64	0.03
160	Figf_p1	Core	868	11	16	0.49	0.03	0.09	Rim	1073	23	0.21	0.09
160	Figf_p2	Core	870	1	17	0.45	0.01	0.09	Rim	947	19	0.27	0.09
160	Figb_p1	Core	879	8	17	0.44	0.1	0.09	Rim	952	18	0.32	0.09
160	Figex_p1	Core	879	13	15	0.55	0.06	0.07	Rim	1015	18	0.43	0.06
160	Fig13_p2	Core	879	7	15	0.61	0.03	0.08	Rim	1013	15	0.61	0.05
160	Fig17_p4	Core	883	8	16	0.55	0.03	0.07	Rim	963	17	0.47	0.08
160	Fig17_p2	Core	892	6	15	0.59	0.03	0.07	Rim	1048	14	0.75	0.03
160	Fig17_p1	Core	894	14	15	0.66	0.08	0.07	Rim	1029	19	0.4	0.07
155	Fig3_p1	Core	903	17	20	0.21	0.11	0.12	Rim	922	21	0.23	0.12
155	Fig24_p1	Core	902	18	21	0.17	0.1	0.13	Rim	900	22	0.2	0.13
149Tb	Fig14_p2	Core	961	6	22	0.36	0.02	0.1	Rim	1008	22	0.45	0.09
149Tb	Fig14_p1	Core	966	6	22	0.39	0.03	0.1	Rim	996	21	0.45	0.09

5.8–9.5 km depths, while the barometer calibrated by Ridolfi and Renzulli (2012) gives pressures equivalent to 5.1–8.4 km depths (each considering a crustal density of 2.8 g/cm<sup>3</sup>; Fowler 2005). These depth ranges have some degree of overlap with the source of co-eruptive subsidence located between 8 and 11 km depth by Delgado et al. (2017). In addition, the barometry results are consistent with the source related to the seismic swarm that occurred a few hours before the eruption, this being a VT event of depth between 7.1 and 7.4 km (SERNAGEOMIN 2015h, i). A summary of inferred depths for the reservoir that fed the eruption is given in Fig. 11. The shallow reservoir suggested in this figure would belong to upper crustal magma storage (Tašárová 2007). This is distinct from the crystallisation of crustal xenoliths at 6–8 kbar (equivalent to depths of 21 to 28 km) reported by Hickey-Vargas et al. (1995) based on amphibole barometry on samples of the 1961 eruption. These results suggest middle to lower crustal storage of the 1961 magma. In several volcanic complexes of the Southern Andes, mush magma reservoirs have been recognised in the upper crust (e.g. at Llaima, Bouvet de Maisonneuve et al. 2012; and Quetrupillán, Brahm et al. 2018). Shallow reservoirs in the Southern Volcanic Zone of the Andes have also been inferred via changes in rigidity of the upper crust (Morgado et al. 2017) and the compressive intra-arc tectonic setting (Cembrano and Lara 2009; Chaussard and Amelung 2012). Together, these results suggest that a complex system of chambers extending from deep to shallow levels may be commonplace at Andean volcanoes.

### Shape and heterogeneity of the reservoir

Delgado et al. (2017) have suggested a prolate, pressurised spheroid shape for the reservoir beneath Calbuco volcano via modelling of the co-eruptive subsidence signal. According to the time-dependent numerical modelling of an evolving magma chamber by Gutiérrez and Parada (2010), thermal heterogeneities are much more likely in stock-like than sill-shaped chambers. Considering long-term thermometry (via two-pyroxenes, amphibole-plagioclase, amphibole and Ca-in-olivine geothermometers; see Tables 5 and 6), sample Cal-160 shows systematically lower temperatures than all other samples (Fig. 10). Fe–Ti oxides thermometry is commonly used to estimate immediately pre-eruptive temperatures (this being ‘short-term thermometry’—Ruprecht and Bachmann 2010; Brahm et al. 2018), and here sample Cal-160 shows systematically lower temperatures for core–core equilibria of in-contact ilmenite–titanomagnetite pairs (see Table 7).

According to Gutiérrez and Parada (2010), in modelling of stock-like reservoirs, the highest temperatures related to crystallinities of between 30 and 40 vol.% are found in the middle of the reservoir. This is a feature of all samples except Cal-160. Instead, lower temperatures related to crystallinities of ~60 vol.% are found at the bottom of the reservoir, as is consistent with features of sample Cal-160. In addition, sample Cal-160 is slightly more evolved than all other samples (lower Mg# and higher SiO<sub>2</sub> wt.%; see Fig. 3). This, according to the Gutiérrez and Parada (2010) modelling, is also consistent with the location of Cal-160 in the lower zone or at the borders of the magma chamber.

## Local-scale heating

In-contact ilmenite–titanomagnetite pairs exchange elements (e.g.  $\text{Fe}^{2+} + \text{Ti}^{4+} \leftrightarrow 2\text{Fe}^{3+}$ ; Ghiorso and Sack 1991) across the interface, which can be used as thermometer and oxygen barometer (Ghiorso and Evans 2008; Sauerzapf et al. 2008). As a consequence, such boundaries respond rapidly to changes in the intensive physical properties of temperature and/or oxygen fugacity within the reservoir (Lasaga 1983). Therefore, we can postulate that crystal core compositions may represent older, relatively long-term temperatures, whereas rim compositions give information of changes of temperature over a short time-scale immediately before eruption.

Rim compositions (close to the interface of the crystal pairs) yield considerably higher temperatures than core compositions only in the sample Cal-160 (70 to 220 °C higher relative to crystal cores; Table 7). The remaining samples show similar Fe–Ti oxides temperatures for cores and rims, with no late heating stage. Additionally, the compositional zonations in orthopyroxene, clinopyroxene and plagioclase phenocrysts (see Figs. 5, 6 and 9) are within the crystal clots as well as in contact with the groundmass, suggesting these zonings were inherited from the crystal mush development stage. This development period would not be associated with zoning due to an ionic exchange as response to the same heating as Fe–Ti oxides recorded because the silicate phases have much lower ionic diffusivities and record older stages of the evolution of the system.

Sample Cal-160 is unique across the sampled deposits as being the only material that records evidence of heating. Its composition and crystallinity make it representative of the bottom of the mush reservoir. The heating that this sample records seems both localised and intense, consistent with an input of hotter magma. Underlying recharge of hot magma has been suggested as a trigger for many eruptions of Southern Andean shallow reservoirs (e.g. Quizapu, Ruprecht and Bachmann 2010; Villarrica, Lohmar et al. 2012, Morgado et al. 2015). Some eruptions have also involved the presence of a mush zone (e.g. Llaima, Bouvet de Maisonneuve et al. 2012; Quetupillán, Brahm et al. 2018). The nature and extent of magma mixing in such situations has been further proposed to influence eruptive style: Ruprecht and Bachmann (2010) suggested that increasing degrees of magma mixing (between felsic magma and a more mafic recharge) decreases the fragmentation efficiency and magma viscosity, and thus favours effusive eruptions. Restricted compositional interaction between the new magma influx and an overlying crystal mush could occur because of the mush acting (at least initially) as a rheological barrier (Huber et al. 2009; Kent et al. 2010) or because of the occurrence of a volatile layer between the hot magma and the crystal mush (Bachmann and Bergantz 2006; Huber et al. 2010b; Parmigiani et al. 2014; Schleicher and Bergantz 2017; Spera and Bohrson 2018). In this situation, only small magma volumes could

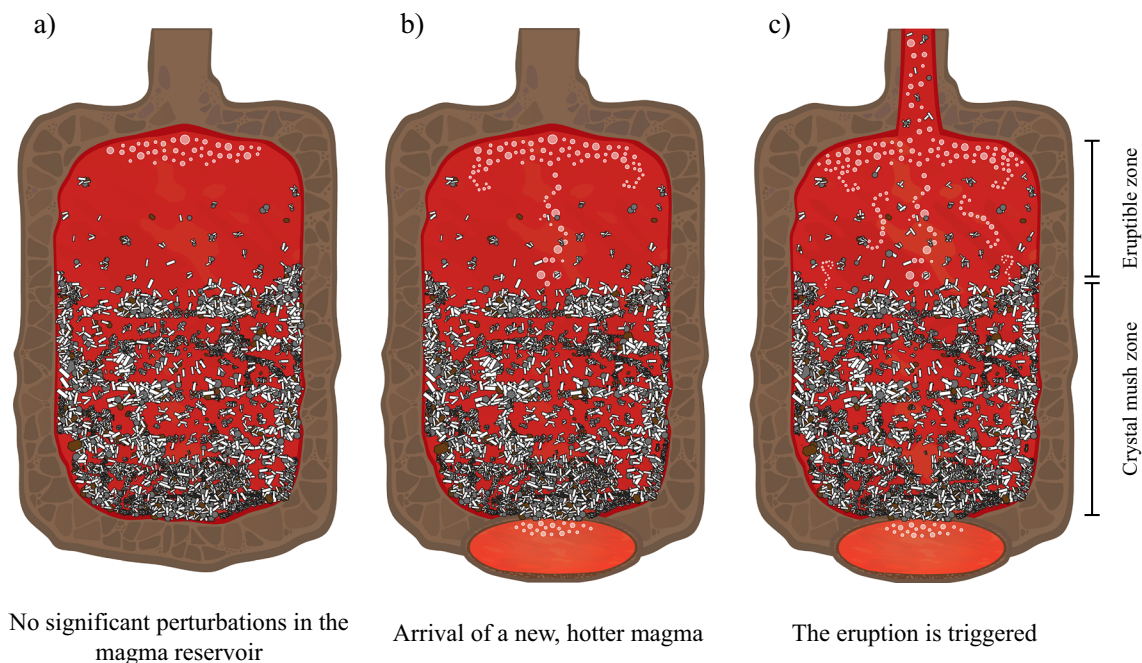


**Fig. 12** Schematic representation of the shape, and evolution in time, of the magma reservoir beneath Calbuco volcano; (a) represents the reservoir, including a mush zone at the bottom, before the input of new

magma; (b) represents the arrival of the new, hotter magma generating a local-scale heating; (c) represents the moment of eruption triggering

be reheated, favouring explosive eruptions (cf. Couch et al. 2001; Ruprecht and Bachmann 2010). Data presented here suggest that this was the case for the April 2015 Calbuco eruption. Our results are consistent with those from Castruccio et al. (2016) who, based on stratigraphy and whole-rock geochemistry, suggested that the April 2015 Calbuco eruption was triggered by either volatile exsolution or a moderate-sized magmatic intrusion of a new magma into the base of the reservoir with almost no mixing effects.

## Conclusions

The 2015 Calbuco eruption is an example of a shallow, crystal-rich magma reservoir feeding a moderate-sized eruption ( $\sim 0.3\text{--}0.6\text{ km}^3$  erupted products, non-DRE). Based on textural and compositional criteria of nine representative samples, we conclude the existence of a mush reservoir, which amphibole barometry indicates to lie within the upper to middle crust (at 5.5–9.5 km depth), consistent with previous works (SERNAGEOMIN 2015h, i; Delgado et al. 2017).

A prolate spheroid shape of the reservoir has been inferred from previous studies and, based on detailed thermobarometry, crystallinity and the compositions of nine representative samples, we infer that all samples of this study (except Cal-160) are derived from the middle of a mush reservoir. Sample Cal-160 represents a portion of the rheologically rigid basal envelope. In addition, based on Fe–Ti oxide (ilmenite and titanomagnetite) thermometry and textural features of the crystal-clot-rich Cal-160 sample, we identify a localised heating event of 70–220 °C, reaching potentially as high as 1070 °C. This mobilised magma represented by Cal-160, an event which we infer to be linked to eruption triggering (Fig. 12) and that would have affected only the magma reservoir at its highly crystalline (mush) base. The absence of a heating record in the remaining samples suggests that all other magma remained thermally and chemically unaffected by the trigger pulse during eruption. This emphasises the need for rapid warning systems to communicate hazards rapidly to the local population.

**Acknowledgements** We acknowledge the help in the field of Marcela Vollmer. We acknowledge Richard Walshaw for assistance with the EPMA, and Duncan Hedges who provided assistance with the SEM at the University of Leeds. Financial support through FONDAP project 15090013 (Centro de Excelencia en Geotermia de los Andes, CEGA), CONICYT MSc fellowship (22141497, RB) and CONICYT PhD fellowship (72160268, EM) are acknowledged. We would like to specially thank to Claire Harnett. We thank two anonymous reviewers for their detailed and constructive comments. Editorial handling and constructive comments of L. Pioli and A. Harris are greatly appreciated.

**Open Access** This article is distributed under the terms of the Creative Commons Attribution 4.0 International License (<http://creativecommons.org/licenses/by/4.0/>), which permits unrestricted use, distribution, and reproduction in any medium, provided you give appropriate credit to the original author(s) and the source, provide a link to the Creative Commons license, and indicate if changes were made.

## References

- Adriasola AC, Thomson SN, Brix MR, Hervé F, Stöckhert B (2006) Postmagmatic cooling and late Cenozoic denudation of the north Patagonian batholith in the Los Lagos region of Chile, 41–42 15' S. *Int J Earth Sci* 95(3):504–528. <https://doi.org/10.1007/s00531-005-0027-9>
- Aggarwal S, Dieckmann R (2002a) Point defects and cat ion tracer diffusion in  $(\text{Ti}_x\text{Fe}_{1-x})_{3-8}\text{O}_4$ . I. Non-stoichiometry and point defects. *Phys Chem Miner* 29(10):695–706. <https://doi.org/10.1007/s00269-002-0282-2>
- Aggarwal S, Dieckmann R (2002b) Point defects and cation tracer diffusion in  $(\text{Ti}_x\text{Fe}_{1-x})_{3-8}\text{O}_4$ . II. Cation tracer diffusion. *Phys Chem Miner* 29(10):707–718. <https://doi.org/10.1007/s00269-002-0284-0>
- Aragon R, McCallister RH, Harrison HR (1984) Cation diffusion in titanomagnetites. *Contrib Mineral Petr* 85(2):174–185. <https://doi.org/10.1007/BF00371707>
- Bachmann O, Bergantz GW (2004) On the origin of crystal-poor rhyolites: extracted from a batholithic crystal mushes. *J Petrol* 45(8): 1565–1582. <https://doi.org/10.1093/petrology/egh019>
- Bachmann O, Bergantz GW (2006) Gas percolation in upper-crustal silicic crystal mushes as a mechanism for upward heat advection and rejuvenation of near-solidus magma bodies. *J Volcanol Geotherm Res* 149(1):85–102. <https://doi.org/10.1016/j.jvolgeores.2005.06.002>
- Bachmann O, Bergantz G (2008) The magma reservoirs that feed supereruptions. *Elements* 4(1):17–21. <https://doi.org/10.2113/GSELEMENTS.4.1.17>
- Bouvet De Maisonneuve C, Dungan MA, Bachmann O, Burgisser A (2012) Insights into shallow magma storage and crystallization at Volcán Llaima (Andean southern volcanic zone, Chile). *J Volcanol Geotherm Res* 211:76–91. <https://doi.org/10.1016/j.jvolgeores.2011.09.010>
- Brahm R, Parada MA, Morgado E, Contreras C, McGee L (2018) Origin of trachyte lavas of the Quetrupillán volcanic complex, Chile (39°30'S): examples of residual melts in rejuvenated crystalline mush reservoir. *J Volcanol Geotherm Res* 357:163–176. <https://doi.org/10.1016/j.jvolgeores.2018.04.020>
- Brey GP, Köhler T (1990) Geothermobarometry in four-phase Lherzolites II. New thermobarometers, and practical assessment of existing thermobarometers. *J Petrol* 31(6):1353–1378. <https://doi.org/10.1093/petrology/31.6.1353>
- Burgisser A, Bergantz GW (2011) A rapid mechanism to remobilize and homogenize highly crystalline magma bodies. *Nature* 471:212–216. <https://doi.org/10.1038/nature09799>
- Castruccio A, Clavero J, Rivera A (2010) Comparative study of lahars generated by the 1961 and 1971 eruptions of Calbuco and Villarrica volcanoes, southern Andes of Chile. *J Volcanol Geotherm Res* 190(3–4):297–311. <https://doi.org/10.1016/j.jvolgeores.2009.12.005>
- Castruccio A, Clavero J, Segura A, Samaniego P, Roche O, Le Pennec J, Drogue B (2016) Eruptive parameters and dynamics of the April 2015 sub-Plinian eruptions of Calbuco volcano (southern Chile). *Bull Volcanol* 327:469–483. <https://doi.org/10.1007/s00445-016-1058-8>



- Cembrano J, Lara L (2009) The link between volcanism and tectonics in the southern volcanic zone of the Chilean Andes: a review. *Tectonophysics* 471(1–2):96–113. <https://doi.org/10.1016/j.tecto.2009.02.038>
- Cembrano J, Hervé F, Lavenue A (1996) The Lique Ofqui fault zone: a long-lived intra-arc fault system in southern Chile. *Tectonophysics* 259(1–3):55–66. [https://doi.org/10.1016/0040-1951\(95\)00066-6](https://doi.org/10.1016/0040-1951(95)00066-6)
- Cembrano J, Schermer E, Lavenue A, Sanhueza A (2000) Contrasting nature of deformation along an intra-arc shear zone, the Lique Ofqui fault zone, southern Chilean Andes. *Tectonophysics* 319: 219–149. [https://doi.org/10.1016/S0040-1951\(99\)00321-2](https://doi.org/10.1016/S0040-1951(99)00321-2)
- Chaussard E, Amelung F (2012) Precursory inflation of shallow magma reservoirs at west Sunda volcanoes detected by InSAR. *Geophys Res Lett* 39(21). <https://doi.org/10.1029/2012GL053817>
- Claiborne LL, Miller CF, Flanagan DM, Clynne MA, Wooden JL (2010) Zircon reveals protracted magma storage and recycling beneath Mount St. Helens. *Geology* 38(11):1011–1014. <https://doi.org/10.1130/G31285.1>
- Cooper KM, Kent AJ (2014) Rapid remobilization of magmatic crystals kept in cold storage. *Nature* 506(7489):480–483. <https://doi.org/10.1038/nature12991>
- Cooper GF, Morgan DJ, Wilson CJ (2017) Rapid assembly and rejuvenation of a large silicic magmatic system: insights from mineral diffusive profiles in the kidnappers and Rocky Hill deposits, New Zealand. *Earth Planet Sci Lett* 473:1–13. <https://doi.org/10.1016/j.epsl.2017.05.036>
- Couch S, Sparks RSJ, Carroll MR (2001) Mineral disequilibrium in lavas explained by convective self-mixing in open magma chambers. *Nature* 411(6841):1037–1039. <https://doi.org/10.1038/35082540>
- Daga R, Ribeiro Guevara S, Poire DG, Arribère M (2014) Characterization of tephra dispersed by the recent eruptions of volcanoes Calbuco (1961), Chaitén (2008) and Cordón Caulle complex (1960 and 2011), in northern Patagonia. *J S Am Earth Sci* 49:1–14. <https://doi.org/10.1016/j.jsames.2013.10.006>
- Dalton JA, Lane SJ (1996) Electron microprobe analysis of Ca in olivine close to grain boundaries: the problem of secondary X-ray fluorescence. *Am Mineral* 81(1–2):194–201. <https://doi.org/10.2138/am-1996-1-224>
- Delgado F, Pritchard ME, Ebmeier S, González P, Lara L (2017) Recent unrest (2002–2015) imaged by space geodesy at the highest risk Chilean volcanoes: Villarrica, Llaima, and Calbuco (southern Andes). *J Volcanol Geotherm Res* 344:270–288. <https://doi.org/10.1016/j.jvolgeores.2017.05.020>
- Dohmen R, Chakraborty S (2007a) Fe–Mg diffusion in olivine I: experimental determination between 700 and 1,200 °C as a function of composition, crystal orientation and oxygen fugacity. *Phys Chem Miner* 34:389–407. <https://doi.org/10.1007/s00269-007-0157-7>
- Dohmen R, Chakraborty S (2007b) Fe–Mg diffusion in olivine II: point defect chemistry, change of diffusion mechanisms and a model for calculation of diffusion coefficients in natural olivine. *Phys Chem Miner* 34:409–430. <https://doi.org/10.1007/s00269-007-0158-6>
- Dohmen R, Ter Heege JH, Becker HW, Chakraborty S (2016) Fe–Mg interdiffusion in orthopyroxene. *Am Mineral* 101(10):2210–2221. <https://doi.org/10.2138/am-2016-5815>
- Droop GTR (1987) A general equation for estimating Fe<sup>3+</sup> concentrations in ferromagnesian silicates and oxides from microprobe analyses, using stoichiometric criteria. *Mineral Mag* 51:431–435
- Fischer O (1893) Erupción del volcán Calbuco, Santiago. *Anales de la Universidad de Chile LXXXV*, pp 197–204
- Fowler CMR (2005) The solid earth: an introduction to global geophysics, 2nd edn. Cambridge University Press, Cambridge
- Ganguly J, Tazzoli V (1994) Fe<sup>2+</sup>–Mg interdiffusion in orthopyroxene: retrieval from the data on intracrystalline exchange reaction. *Am Mineral* 79(9–10):930–937
- Ghiorso MS, Evans BW (2008) Thermodynamics of rhombohedral oxide solid solutions and a revision of the Fe–Ti two-oxide geothermometer and oxygen-barometer. *Am J Sci* 308:957–1039. <https://doi.org/10.2475/09.2008.01>
- Ghiorso MS, Sack O (1991) Fe–Ti oxide geothermometry: thermodynamic formulation and the estimation of intensive variables in silicic magmas. *Contrib Mineral Petr* 108(4):485–510. <https://doi.org/10.1007/BF00303452>
- Ghiorso MS, Sack RO (1995) Chemical mass transfer in magmatic processes IV. A revised and internally consistent thermodynamic model for the interpolation and extrapolation of liquid–solid equilibria in magmatic systems at elevated temperatures and pressures. *Contrib Mineral and Petr* 119(2–3):197–212. <https://doi.org/10.1007/BF00307281>
- Grove TL, Baker MB, Kinzler RJ (1984) Coupled CaAl–NaSi diffusion in plagioclase feldspar: experiments and applications to cooling rate speedometry. *Geochim Cosmochim Acta* 48(10):2113–2121. [https://doi.org/10.1016/0016-7037\(84\)90391-0](https://doi.org/10.1016/0016-7037(84)90391-0)
- Grove TL, Donnelly-Nolan JM, Housh T (1997) Magmatic processes that generated the rhyolite of Glass Mountain, Medicine Lake Volcano, N. California. *Contrib Mineral Petrol* 127(3):205–223. <https://doi.org/10.1007/s004100050276>
- Gutiérrez F, Parada MA (2010) Numerical modeling of time-dependent fluid dynamics and differentiation of a shallow basaltic magma chamber. *J Petrol* 51(3):731–762. <https://doi.org/10.1093/petrology/egp101>
- Hickey-Vargas R, Abdollahi MJ, Parada MA, López-Escobar L, Frey FA (1995) Crustal xenoliths from Calbuco volcano, Andean southern volcanic zone: implications for crustal composition and magma–crust interaction. *Contrib Mineral Petr* 119(4):331–344. <https://doi.org/10.1007/BF00286933>
- Hildreth W (2004) Volcanological perspectives on Long Valley, Mammoth Mountain, and mono craters: several contiguous but discrete systems. *J Volcanol Geotherm Res* 136(3):169–198. <https://doi.org/10.1016/j.jvolgeores.2004.05.019>
- Holland T, Blundy J (1994) Non-ideal interactions in calcic amphiboles and their bearing on amphibole–plagioclase thermometry. *Contrib Mineral Petrol* 116(4):433–447. <https://doi.org/10.1007/BF00310910>
- Huber C, Bachmann O, Manga M (2009) Homogenization processes in silicic magma chambers by stirring and mushification (latent heat buffering). *Earth Planet Sci Lett* 283(1):38–47. <https://doi.org/10.1016/j.epsl.2009.03.029>
- Huber C, Bachmann O, Dufek J (2010a) The limitations of melting on the reactivation of silicic mushes. *J Volcanol Geotherm Res* 195(2):97–105. <https://doi.org/10.1016/j.jvolgeores.2010.06.006>
- Huber C, Bachmann O, Manga M (2010b) Two competing effects of volatiles on heat transfer in crystal-rich magmas: thermal insulation vs defrosting. *J Petrol* 51(4):847–867. <https://doi.org/10.1093/petrology/egq003>
- Irvine TNJ, Baragar WRAF (1971) A guide to the chemical classification of the common volcanic rocks. *Can J Earth Sci* 8(5):523–548. <https://doi.org/10.1139/e71-055>
- Ivy DJ, Solomon S, Kinnison D, Mills MJ, Schmidt A, Neely RR (2017) The influence of the Calbuco eruption on the 2015 Antarctic ozone hole in a fully coupled chemistry–climate model. *Geophys Res Lett* 44:1–6. <https://doi.org/10.1002/2016GL071925>
- Kent AJ, Darr C, Koleszar AM, Salisbury MJ, Cooper KM (2010) Preferential eruption of andesitic magmas through recharge filtering. *Nat Geosci* 3(9):631–636. <https://doi.org/10.1038/ngeo924>
- Klohn E (1963) The February 1961 eruption of Calbuco volcano. *B Seismol Soc Am* 53(6):1435–1436
- Koyaguchi T, Kaneko K (1999) A two-stage thermal evolution model of magmas in continental crust. *J Petrol* 40(2):241–254. <https://doi.org/10.1093/petroj/40.2.241>
- Lahsen, A, Moreno, H, Varela, J, Munizaga, F, López, L (1985) Geología y riesgo volcánico del volcán Calbuco y centros eruptivos menores. *Proy Canutillar, ENDESA-Univ Chile, Informe Técnico*, 215p



- Lara, LE, Orozco, G, Amigo, Á, Silva, C (2011) Peligros Volcánicos de Chile, Servicio Nacional de Geología y Minería, Carta Geológica de Chile, Serie Geología Ambiental. No. 13:34, Mapa escala 1: 2.000.000. Santiago
- Lasaga AC (1983) Geospeedometry: an extension of geothermometry. In: Saxena SK (ed) Kinetics and equilibrium in mineral reactions. In: Advances in physical geochemistry, vol. 3. Springer, New York, pp 81–114
- Le Bas ML, Maitre RL, Streckeisen A, Zanettin B (1986) IUGS subcommission on the systematics of igneous rocks. A chemical classification of volcanic rocks based on the total alkali-silica diagram. *J Petrol* 27(3):745–750. <https://doi.org/10.1093/petrology/27.3.745>
- Leake BE, Woolley AR, Arps CES, Birch WD, Gilbert MC, Grice JD, Hawthorne FC, Kato A, Kisch HJ, Krivovichev VG, Linthout K, Laird J, Mandarino JA, Maresch WV, Nickel EH, Rock NMS, Schumacher JC, Smith DC, Stephenson NCN, Ungaretti L, Whittaker EJW, Youzhi G (1997) Nomenclature of amphiboles: report of the subcommittee on amphiboles of the International Mineralogical Association, Commission on New Minerals and Mineral Names. *Can Mineral* 35:219–246
- Lohmar S, Parada M, Gutiérrez F, Robin C, Gerbe MC (2012) Mineralogical and numerical approaches to establish the pre-eruptive conditions of the mafic Lican ignimbrite, Villarrica volcano (Chilean southern Andes). *J Volcanol Geotherm Res* 235:55–69. <https://doi.org/10.1016/j.jvolgeores.2012.05.006>
- López-Escobar L, Parada MÁ, Moreno H, Frey FA, Hickey-Vargas RL (1992) A contribution to the petrogenesis of Osorno and Calbuco volcanoes, Southern Andes (41°00'–41°30' S): comparative study. *Rev Geol Chile* 19(2):211–226
- López-Escobar L, Cembrano J, Moreno H (1995a) Geochemistry and tectonics of the Chilean southern Andes basaltic quaternary volcanism (37–46° S). *Rev Geol Chile* 22(2):219–234
- López-Escobar L, Parada MÁ, Hickey-Vargas R, Frey FA, Kempton PD, Moreno H (1995b) Calbuco volcano and minor eruptive centers distributed along the Liquiñe–Ofqui fault zone, Chile (41°–42° S): contrasting origin of andesitic and basaltic magma in the southern volcanic zone of the Andes. *Contrib Mineral Pet* 119:345–336. <https://doi.org/10.1007/BF00286934>
- Marsh BD (1989) Magma chambers. *Annu Rev Earth Pl Sc* 17(1):439–472. <https://doi.org/10.1146/annurev.earth.17.050189.002255>
- Marsh BD (1996) Solidification fronts and magmatic evolution. *Mineral Mag* 60(1):5–40. <https://doi.org/10.1180/minmag.1996.060.398.03>
- Molina PG, Parada MÁ, Gutiérrez FJ, Ma C, Li J, Yuanyuan L, Reich M, Aravena Á (2015) Protracted late magmatic stage of the Caleu pluton (Central Chile) as a consequence of heat redistribution by diiking: insights from zircon data and thermal modeling. *Lithos* 227:255–268. <https://doi.org/10.1016/j.lithos.2015.04.008>
- Moore A, Coogan LA, Costa F, Perfit MR (2014) Primitive melt replenishment and crystal-mush disaggregation in the weeks preceding the 2005–2006 eruption 9° 50' N, EPR. *Earth Planet Sci Lett* 403:15–26. <https://doi.org/10.1016/j.epsl.2014.06.015>
- Moreno H, Naranjo JA, Clavero J (2006) Generación de lahares calientes en el volcán Calbuco, Andes del sur de Chile (41,3°S). In *Actas XI Congreso Geológico Chileno* 2:512–513
- Morgado E, Parada MÁ, Contreras C, Castruccio A, Gutiérrez F, McGee L (2015) Contrasting records from mantle to surface of two nearby arc volcanic complexes: Caburgua–Huelmolle small eruptive centers and Villarrica volcano. *J Volcanol Geotherm Res* 306:1–16. <https://doi.org/10.1016/j.jvolgeores.2015.09.023>
- Morgado E, Parada MÁ, Morgan DJ, Gutiérrez F, Castruccio A, Contreras C (2017) Transient shallow reservoirs beneath small eruptive centres: constraints from Mg–Fe interdiffusion in olivine. *J Volcanol Geotherm Res* 347:327–336. <https://doi.org/10.1016/j.jvolgeores.2017.10.002>
- Müller T, Dohmen R, Becker HW, Ter Heege JH, Chakraborty S (2013) Fe–Mg interdiffusion rates in clinopyroxene: experimental data and implications for Fe–Mg exchange geothermometers. *Contrib Mineral Petr* 166(6):1563–1576. <https://doi.org/10.1007/s00410-013-0941-y>
- Parada MÁ (1990) Composición de fenocristales en lavas en volcán Calbuco y sus implicancias en la historia temprana de cristalización. *Actas XI Congreso Geológico Argentino* 1:101–104
- Parmigiani A, Huber C, Bachmann O (2014) Mush microphysics and the reactivation of crystal-rich magma reservoirs. *J Geophys Res Solid Earth* 119(8):6308–6322. <https://doi.org/10.1002/2014JB011124>
- Passmore E, MacLennan J, Fittton G, Thordarson T (2012) Mush disaggregation in basaltic magma chambers: evidence from the AD 1783 Laki eruption. *J Petrol* 53(12):2593–2623. <https://doi.org/10.1093/petrology/egs061>
- Petit-Breuilh ME (1999) Cronología eruptiva histórica de los volcanes Osorno y Calbuco, Andes del Sur (41°–41°30'S). *Boletín no. 53*. Servicio Nacional de Geología y Minería, 46 p
- Putirka KD (2008) Thermometers and barometers for volcanic systems. *Rev Mineral Geochem* 69(1):61–120. <https://doi.org/10.2138/rmg.2008.69.3>
- Ridolfi F, Renzulli A (2012) Calcic amphiboles in calc-alkaline and alkaline magmas: thermobarometric and chemometric empirical equations valid up to 1,130 °C and 2.2 GPa. *Contrib Mineral Petrol* 163: 877–895. <https://doi.org/10.1007/s00410-011-0704-6>
- Ridolfi F, Renzulli A, Puerini M (2010) Stability and chemical equilibrium of amphibole in calc-alkaline magmas: an overview, new thermobarometric formulations and application to subduction-related volcanoes. *Contrib Mineral Petrol* 160(1):45–66. <https://doi.org/10.1007/s00410-009-0465-7>
- Romero JE, Morgavi D, Arzilli F, Daga R, Caselli A, Reckziegel F, Viramonte J (2016) Eruption dynamics of the 22–23 April 2015 Calbuco volcano (southern Chile): analyses of tephra fall deposits. *J Volcanol Geotherm Res* 317:15–29. <https://doi.org/10.1016/j.jvolgeores.2016.02.027>
- Ruprecht P, Bachmann O (2010) Pre-eruptive reheating during magma mixing at Quizapu volcano and the implications for the explosiveness of silicic arc volcanoes. *Geology* 38(10):919–922. <https://doi.org/10.1130/G31110.1>
- Sauerzapf U, Lattard D, Burchard M, Engelmann R (2008) The titanomagnetite–ilmenite equilibrium: new experimental data and thermo-oxybarometric application to the crystallization of basic to intermediate rocks. *J Petrol* 49(6):1161–1185. <https://doi.org/10.1093/petrology/egn021>
- Saunders KE, Morgan DJ, Baker JA, Wysoczanski RJ (2010) The magmatic evolution of the Whakamaru supereruption, New Zealand, constrained by a microanalytical study of plagioclase and quartz. *J Petrol* 51(12):2465–2488. <https://doi.org/10.1093/petrology/egq064>
- Schleicher JM, Bergantz GW (2017) The mechanics and temporal evolution of an open-system magmatic intrusion into a crystal-rich magma. *J Petrol* 58:1059–1072. <https://doi.org/10.1093/petrology/egx045>
- Sellés, D, Moreno, H (2011) Geología del Volcán Calbuco, Región de Los Lagos. Carta Geológica de Chile. Serie Geológica Básica, No. 130. Escala 1:50.000
- SERNAGEOMIN (2015a) Reporte especial de actividad volcánica (REAV)—Región de los Lagos, 2015, Abril 22—18:00
- SERNAGEOMIN (2015b) Reporte especial de actividad volcánica (REAV) - Región de los Lagos, 2015, Abril 22—20:45
- SERNAGEOMIN (2015c) Reporte especial de actividad volcánica (REAV)—Región de los Lagos, 2015, Abril 23—10:30
- SERNAGEOMIN (2015d) Reporte especial de actividad volcánica (REAV)—Región de los Lagos, 2015, Abril 23—01:10
- SERNAGEOMIN (2015e) Reporte especial de actividad volcánica (REAV)—Región de los Lagos, 2015, Abril 22—22:30
- SERNAGEOMIN (2015f) Reporte especial de actividad volcánica (REAV)—Región de los Lagos, 2015, Abril 22—17:30

- SERNAGEOMIN (2015g) Reporte especial de actividad volcánica (REAV)—Región de los Lagos, 2015, Abril 23—10.30
- SERNAGEOMIN (2015h) Reporte especial de actividad volcánica (REAV)—Región de los Lagos, 2015, Abril 22
- SERNAGEOMIN (2015i) Reporte especial de actividad volcánica (REAV)—Región de los Lagos, 2015, Abril—Volumen 4a
- SERNAGEOMIN (2017) Red Nacional de Vigilancia Volcánica, Volcán Calbuco. <http://www.sernageomin.cl/volcan-calbuco>. Accessed 3 March 2019
- SERNAGEOMIN – BRGM (1995) Carta metalogénica X Región Sur, Chile. Servicio Nacional de Geología y Minería, Informe Registrado IR-95-05 (Inédito), 4 tomos, Santiago
- Shejwalkar A, Coogan LA (2013) Experimental calibration of the roles of temperature and composition in the Ca-in-olivine geothermometer at 0.1 MPa. *Lithos* 177:54–60. <https://doi.org/10.1016/j.lithos.2013.06.013>
- Spera FJ, Bohron WA (2018) Rejuvenation of crustal magma mush: a tale of multiply nested processes and timescales. *Am J Sci* 318:90–140. <https://doi.org/10.2475/01.2018.05>
- Stern CR, Moreno H, López-Escobar L, Clavero JE, Lara LE, Naranjo JA, Parada MÁ, Skewes MA (2007) Chilean Volcanoes. In: Moreno T, Gibbons W (eds) *The geology of Chile*. Geological Society of London, London, pp 149–180
- Stormer JC (1983) The effects of recalculation on estimates of temperature and oxygen fugacity from analyses of multicomponent iron–titanium oxides. *Am Mineral* 68:586–594
- Sun SS, McDonough WS (1989) Chemical and isotopic systematics of oceanic basalts: implications for mantle composition and processes. *Geol Soc Lond, Spec Publ* 42(1):313–345. <https://doi.org/10.1144/GSL.SP.1989.042.01.19>
- Szymanowski D, Wotzlaw JF, Ellis BS, Bachmann O, Guillong M, von Quadt A (2017) Protracted near-solidus storage and pre-eruptive rejuvenation of large magma reservoirs. *Nat Geosci* 10:777–782. <https://doi.org/10.1038/NGEO3020>
- Tašárová ZA (2007) Towards understanding the lithospheric structure of the southern Chilean subduction zone (36°S–42°S) and its role in the gravity field. *Geophys J Int* 170(3):995–1014. <https://doi.org/10.1111/j.1365-246X.2007.03466.x>
- Thiele, R, Godoy, E, Parada, MÁ, Varela, J (1985) Estudio geológico-estructural regional y tectónico del área Petrohué-Canutillar. Proyecto Petrohué-Canutillar, ENDESA-U. de Chile (unpublished report)
- Valderrama, Ó, Franco, L, Gil-Cruz, F (2015) Erupción intempestiva del volcán Calbuco, Abril 2015, XIV Congreso Geológico Chileno, III, p. 91–93
- Van Eaton AR, Amigo Á, Bertin D, Mastin LG, Giacosa RE, González J, Valderrama Ó, Fontijn K, Behnke SA (2016) Volcanic lightning and plume behavior reveal evolving hazards during the April 2015 eruption of Calbuco volcano, Chile. *Geophys Res Lett* 43(7):3563–3571. <https://doi.org/10.1002/2016GL068076>
- Watt SF, Pyle DM, Naranjo JA, Rosqvist G, Mella M, Mather TA, Moreno H (2011) Holocene tephrochronology of the Hualaihue region (Andean southern volcanic zone, ~42°S), southern Chile. *Quatern Int* 246(1):324–343. <https://doi.org/10.1016/j.quaint.2011.05.029>